

Inverse Source Method for Constrained Phased Array Synthesis through Null-Space Exploitation

L. Poli,⁽¹⁾⁽²⁾ *Senior Member, IEEE*, P. Rocca,⁽¹⁾⁽²⁾⁽³⁾ *Fellow, IEEE*, A. Benoni,⁽¹⁾⁽²⁾ *Member, IEEE*, and A. Massa,⁽¹⁾⁽²⁾⁽⁴⁾⁽⁵⁾⁽⁶⁾ *Fellow, IEEE*

⁽¹⁾ *ELEDIA Research Center (ELEDIA@UniTN - University of Trento)*

DICAM - Department of Civil, Environmental, and Mechanical Engineering

Via Mesiano 77, 38123 Trento - Italy

E-mail: {lorenzo.poli, paolo.rocca, arianna.benoni, andrea.massa}@unitn.it

Website: www.eledia.org/eledia-unitn

⁽²⁾ *CNIT - "University of Trento" ELEDIA Research Unit*

Via Mesiano 77, 38123 Trento - Italy

Website: www.eledia.org/eledia-unitn

⁽³⁾ *ELEDIA Research Center (ELEDIA@XIDIAN - Xidian University)*

P.O. Box 191, No.2 South Tabai Road, 710071 Xi'an, Shaanxi Province - China

E-mail: paolo.rocca@xidian.edu.cn

Website: www.eledia.org/eledia-xidian

⁽⁴⁾ *ELEDIA Research Center (ELEDIA@UESTC - UESTC)*

School of Electronic Science and Engineering, Chengdu 611731 - China

E-mail: andrea.massa@uestc.edu.cn

Website: www.eledia.org/eledia-uestc

⁽⁵⁾ *ELEDIA Research Center (ELEDIA@TSINGHUA - Tsinghua University)*

30 Shuangqing Rd, 100084 Haidian, Beijing - China

E-mail: andrea.massa@tsinghua.edu.cn

Website: www.eledia.org/eledia-tsinghua

⁽⁶⁾ *School of Electrical Engineering*

Tel Aviv University, Tel Aviv 69978 - Israel

E-mail: andrea.massa@eng.tau.ac.il

Website: <https://engineering.tau.ac.il/>

This work has been submitted to the IEEE for possible publication. Copyright may be transferred without notice, after which this version may no longer be accessible.

Inverse Source Method for Constrained Phased Array Synthesis through Null-Space Exploitation

L. Poli, P. Rocca, A. Benoni, and A. Massa

Abstract

A versatile approach for the synthesis of phased array (*PA*) antennas able to fit user-defined power pattern masks, while fulfilling additional geometrical and/or electrical constraints on the geometry of the array aperture and/or on the array excitations is presented. Such a synthesis method is based on the *inverse source* (*IS*) formulation and exploits the null-space of the radiation operator that causes the non-uniqueness of the *IS* problem at hand. More in detail, the unknown element excitations of the *PA* are expressed as the linear combination of a *minimum-norm* or *radiating* (*RA*) term and a suitable *non-radiating* (*NR*) component. The former, computed via the truncated singular value decomposition (*SVD*) of the array radiation operator, is devoted to generate a far-field power pattern that fulfills user-defined pattern masks. The other one belongs to the null-space of the radiation operator and allows one to fit additional geometrical and/or electrical constraints on the geometry of the array aperture and/or on the beam-forming network (*BFN*) when determined with a customized global optimization strategy. A set of numerical examples, concerned with various array arrangements and additional design targets, is reported to prove the effectiveness of the proposed approach.

Key words: Phased Array Antenna (*PA*), Power Pattern Synthesis, Inverse Problem (*IP*), Inverse Source (*IS*), Singular Value Decomposition (*SVD*), Optimization Method.

1 Introduction

Phased array (*PA*) antennas have become pivotal devices for high-performance electromagnetic (*EM*) systems across a wide spectrum of applications including radar, satellite communications, wireless networks, remote sensing, and navigation [1]. The capability to produce electronically steerable beams with high precision and gain, combined with rapid reconfigurability, makes *PA*s fundamental assets in both traditional and emerging scenarios where adaptability, efficiency, and compactness are key-issues. As the global demand for connected, intelligent, and resilient infrastructures increases, *PA*s have a central role in non-conventional domains such as autonomous mobility, smart buildings, and distributed sensing platforms. Within this framework, the design of innovative *PA* solutions with tailored geometrical layouts and simplified feeding networks is of paramount interest [2][3].

The synthesis of *PA* antennas - specifically, the determination of suitable excitations to generate prescribed far-field radiation patterns - is still a core challenge. Traditionally, *PA*s synthesis techniques have been mainly focused on fulfilling radiation requirements (namely, “*functional*” requirements) such as matching a target power pattern or minimizing the sidelobe level (*SLL*) [4]-[6] or fitting a power pattern mask [5][6]. However, to address the needs of practical implementations, it is increasingly important to incorporate in the design process additional geometrical and electrical constraints also indicated as “*non-functional*” requirements. They may include enforcing modular or sparse array topologies [7][8], excluding feed points in a set of regions of the *PA* aperture or according to thinned configurations [9][10], or ensuring the compatibility with low-cost and low-power beam-forming networks (*BFNs*) implementations [11][12]. Unfortunately, most conventional approaches to *PA* synthesis neglect or do not inherently deal with these constraints.

To overcome these limitations, this work proposes a novel approach for the synthesis of *PA*s based on an inverse source (*IS*) formulation [13] where the desired radiation pattern and the element excitations are the data and the unknowns of the problem at hand, respectively. By modeling the data-unknowns relationship with the linear radiation operator, according to the Green’s function theory [14], the *PA* synthesis is cast as the inverse problem (*IP*) of determining an excitation vector that fits far-field power constraints. It is well-known that *IS* problems are

ill-posed [15]-[18] owing to the non-uniqueness of the solution, which is a direct consequence of the presence of non-radiating (*NR*) current components, namely *PA* excitations that radiate only within the antenna support and do not contribute to the far-field pattern [19]-[21].

Unlike inverse scattering problems, the non-uniqueness feature of this *IS* problem is not a limitation/issue, but an additional degree of freedom (*DoF*) [22] to fulfill *non-functional* design constraints. More in detail, the *PA* element excitations are expressed as the superposition of two components, namely a minimum-norm or radiating (*RA*) term, which fulfills the *functional* radiation objective, and a tailored *NR* component that allows one to fit additional geometrical and/or electrical constraints. These latter may include, for example, either the presence of “*forbidden*” regions in the *PA* aperture where the excitations are forced to be null or promoting the *BFN* sparsity. The *NR* component is determined through a proper customization of a constrained optimization approach successfully adopted for the design of both surface currents of reflectarrays [23][24] and inexpensive static passive *EM* skins (*SP-EMS*) [25] in the framework of Smart Electromagnetic Environments for next generation communication systems [26][27]. The result is the definition of a flexible and computationally-efficient synthesis method for the delivery of physically meaningful and implementable *PA* layouts without compromising radiation performance. It is worthwhile to point out that the analytical formulation of the *IS* problem at hand enables the definition of suitable representation bases for the *NR* components [28][29] as well as an effective use of a multi-agent global optimization strategy to determine the *NR* expansion coefficients by avoiding local minima traps and reducing the overall computational complexity [30].

To the best of the authors’ knowledge, the main novelties of this work over the existing state-of-the-art literature on *PA* synthesis include (i) a new theoretical framework for the synthesis of *PA* antennas that exploits the non-uniqueness of the *IS* problem at hand to explicitly take advantage of the components of the null-space of the radiation operator, (ii) an innovative method to define the *NR* components of the element excitations for fulfilling user-defined or application-driven geometrical and/or electrical constraints, (iii) the numerical assessment of the effectiveness and the versatility of the proposed *NR*-based array synthesis method when applied to various array arrangements, including linear and planar arrays, and design targets such as the presence of

“forbidden” regions within the antenna aperture as well as the simplification of the *BFN*.

The outline of the paper is as follows. The problem is mathematically formulated in Sect. 2, while the proposed *NR* synthesis method is presented in Sect. 3. Section 4 is devoted to the numerical analysis and the assessment of the proposed approach. Eventually, some conclusions and final remarks are drawn (Sect. 5).

2 Mathematical Formulation

Let us consider a planar *PA* with aperture A lying on the xy plane and composed of N elements centered at $\{(x_n, y_n); n = 1, \dots, N\}$ as shown in Fig. 1. The far-field pattern of the array at the carrier frequency f is given by

$$\mathbf{E}(\theta, \phi) = \sum_{n=1}^N w_n \mathbf{a}_n(\theta, \phi) e^{j \frac{2\pi}{\lambda} (x_n \sin \theta \cos \phi + y_n \sin \theta \sin \phi)} \quad (1)$$

where $w_n = \alpha_n e^{j\beta_n}$ is the complex excitation, with amplitude α_n and phase β_n , of the n -th ($n = 1, \dots, N$) radiating element of the *PA*, which is characterized by an active element pattern $\mathbf{a}_n(\theta, \phi)$. Moreover, λ is the wavelength at f and (θ, ϕ) is the angular direction, θ and ϕ being the angular coordinates ranging within $\theta \in [-90 : 90]$ [deg] and $\phi \in [0 : 180]$ [deg], respectively. In order to assess the feasibility and performance of the array architecture [31] without any *a-priori* assumption on the type of radiating elements in the *PA*, let us consider ideal isotropic radiators in absence of mutual coupling, thus $\mathbf{a}_n(\theta, \phi) = \frac{1}{\sqrt{2}} (\hat{\theta} + \hat{\phi})$ ($n = 1, \dots, N$), $\hat{\theta}$ and $\hat{\phi}$ being unit vectors. Accordingly, the expression in (1) simplifies to the array factor

$$AF(\theta, \phi | \underline{r}, \underline{w}) = \sum_{n=1}^N w_n e^{j \frac{2\pi}{\lambda} (x_n \sin \theta \cos \phi + y_n \sin \theta \sin \phi)}, \quad (2)$$

which is only function of the electrical and geometrical array parameters, namely the excitations set, $\underline{w} = \{w_n; n = 1, \dots, N\}$, and the element positions set, $\underline{r} = \{\mathbf{r}_n = (x_n, y_n); n = 1, \dots, N\}$. In this framework, the formulation of the “standard” array synthesis problem can be stated as follows:

Standard Array Synthesis (SAS) Problem - Given the upper, $UM(\theta, \phi)$, and

the lower, $LM(\theta, \phi)$, power pattern masks and the positions of the N array elements, \underline{r} , define the amplitude, $\underline{\alpha} = \{\alpha_n; n = 1, \dots, N\}$, and the phase, $\underline{\beta} = \{\beta_n; n = 1, \dots, N\}$, values of the set of complex excitations, \underline{w} , of the array so that the radiated power pattern

$$P(\theta, \phi | \underline{w}) = |AF(\theta, \phi | \underline{w})|^2 \quad (3)$$

minimizes the following *mask-matching* metric

$$\begin{aligned} \Phi_M(\theta, \phi | \underline{w}) = & \frac{1}{2\pi} \int_0^{2\pi} \int_0^{\frac{\pi}{2}} \{ [P(\theta, \phi | \underline{w}) - UM(\theta, \phi)] H\{P(\theta, \phi | \underline{w}) - UM(\theta, \phi)\} + \\ & [LM(\theta, \phi) - P(\theta, \phi | \underline{w})] H\{LM(\theta, \phi) - P(\theta, \phi | \underline{w})\} \} \sin \theta d\theta d\phi \end{aligned} \quad (4)$$

aimed at quantifying the violation of $P(\theta, \phi | \underline{w})$ from the upper, $UM(\theta, \phi)$, and the lower, $LM(\theta, \phi)$, pattern masks, $H\{\circ\}$ being the Heaviside step function ($H\{\circ\} = 1$ if $\circ \geq 0$ and $H\{\circ\} = 0$, otherwise).

Various synthesis methods have been successfully developed to address the SAS problem [4]-[6], but even though the arising excitation set typically ensures the compliance with the power mask - provided a physical solution exists - it does not account for additional constraints.

By leveraging on the ill-posedness of the *IS* problems and the non-uniqueness of their solutions, the element excitations can be expressed as

$$\underline{w} = \underline{w}^{RA} + \underline{w}^{NR} \quad (5)$$

where \underline{w}^{RA} ($\underline{w}^{RA} = \{w_n^{RA}; n = 1, \dots, N\}$) is the set of the minimum-norm weights aimed at generating the far-field pattern (2) to fulfill the *functional/primary* problem objective by fitting the mask-matching requirement (4) [i.e., $\Phi_M(\underline{w}^{RA}) = 0$], while \underline{w}^{NR} ($\underline{w}^{NR} = \{w_n^{NR}; n = 1, \dots, N\}$) is the set of non-radiating coefficients generating a null *EM* field outside the aperture A , that is

$$0 = \sum_{n=1}^N w_n^{NR} e^{j\frac{2\pi}{\lambda}(x_n \sin \theta \cos \phi + y_n \sin \theta \sin \phi)} . \quad (6)$$

Therefore, it turns out that $AF(\theta, \phi | \underline{w}) = AF^{RA}(\theta, \phi)$, $AF^{RA}(\theta, \phi)$ being the array factor (2)

when $\underline{w} = \underline{w}^{RA}$ [i.e., $AF^{RA}(\theta, \phi) \triangleq \sum_{n=1}^N w_n^{RA} e^{j\frac{2\pi}{\lambda}(x_n \sin \theta \cos \phi + y_n \sin \theta \sin \phi)}$]. Accordingly, the constrained version of the SAS problem is formulated as follows:

Constrained Array Synthesis (CAS) Problem - Given an array of N elements having positions \underline{r} and excitations \underline{w}^{ref} that affords a reference power pattern $P^{ref}(\theta, \phi)$ [$P^{ref}(\theta, \phi) \triangleq P(\theta, \phi | \underline{w}^{ref})$; $P(\theta, \phi | \underline{w}^{ref}) = |AF(\theta, \phi | \underline{w}^{ref})|^2$] fitting the upper $UM(\theta, \phi)$ and lower $LM(\theta, \phi)$ mask constraints, determine (a) the set of the minimum-norm/radiating weighting coefficients \underline{w}^{RA} , which radiate a MN power pattern $P^{RA}(\theta, \phi)$ [$P^{RA}(\theta, \phi) \triangleq P(\theta, \phi | \underline{w}^{RA})$; $P(\theta, \phi | \underline{w}^{RA}) = |AF(\theta, \phi | \underline{w}^{RA})|^2$] close to the reference one within a certain tolerance ξ

$$\frac{\int_0^{2\pi} \int_0^{\frac{\pi}{2}} |P^{RA}(\theta, \phi) - P^{ref}(\theta, \phi)| \sin \theta d\theta d\phi}{\int_0^{2\pi} \int_0^{\frac{\pi}{2}} P^{ref}(\theta, \phi) \sin \theta d\theta d\phi} \leq \xi; \quad (7)$$

(b) the set of non-radiating coefficients \underline{w}^{NR} so that additional user-defined geometrical and/or electrical constraints, coded into a dedicated objective function $\Phi_C(\underline{w})$ to be minimized, are fulfilled.

3 NR Current Based Constrained Array Synthesis (NR-CAS)

Method

In order to exploit the non-uniqueness of the *IS* problem at hand and the existence of the *NR* currents as additional *DoFs*, the *CAS* problem is numerically solved through the procedure sketched in Fig. 2 and detailed in the following:

- **Step 1 - EM Field Discretization.** Discretize the angular domain into M samples ($M \geq N$) and fill the vector \underline{AF} whose m -th ($m = 1, \dots, M$) entry is $AF(\theta_m, \phi_m)$, compute the radiation operator matrix $\mathcal{G} = \{g_{mn}; m = 1, \dots, M; n = 1, \dots, N\}$ of dimensions $M \times N$, whose (m, n) -th ($m = 1, \dots, M; n = 1, \dots, N$) complex-valued entry is

$$g_{mn} = e^{j\frac{2\pi}{\lambda}[(x_n \sin \theta_m \cos \phi_m + y_n \sin \theta_m \sin \phi_m)]}, \quad (8)$$

to rewrite (2) in matrix form, that is $\underline{AF} = \mathcal{G}\underline{w}$;

- **Step 2 - SVD of Radiation Operator.** Perform the singular value decomposition (SVD) of the radiation operator matrix, \mathcal{G} ,

$$\mathcal{G} = \mathcal{U}\Sigma\mathcal{V}^*, \quad (9)$$

\mathcal{U} and \mathcal{V} being the matrices whose m -th ($m = 1, \dots, M$) and n -th ($n = 1, \dots, N$) columns are the left, \underline{u}_m , and the right, \underline{v}_n , singular vectors, respectively, of unit norm (i.e., $\|\underline{u}_m\|_2 = 1, \forall m; \|\underline{v}_n\|_2 = 1, \forall n$) and orthogonal (i.e., $\langle \underline{u}_m, \underline{u}_l \rangle = 0, \forall m, l = 1, \dots, M, m \neq l; \langle \underline{v}_n, \underline{v}_l \rangle = 0, \forall n, l = 1, \dots, N, n \neq l$, $\langle \cdot, \cdot \rangle$ being the scalar product). In (9), $\Sigma = \text{diag} \{ \sigma_n; n = 1, \dots, N \}$ is the diagonal matrix whose non-null entries are the N singular values listed in descending order (i.e., $\sigma_n \geq \sigma_{n+1}, n = 1, \dots, N-1$) and \cdot^* stands for conjugate transpose;

- **Step 3 - MN Excitations Definition.** Compute the radiating coefficients as follows

$$\underline{w}^{RA} = \sum_{s=1}^S \frac{1}{\sigma_s} \langle \underline{u}_s^*, \underline{AF}^{ref} \rangle \underline{v}_s \quad (10)$$

where $S = \arg \max_{n=1, \dots, N} \{ \hat{\sigma}_n > \chi \}$ ($\hat{\sigma}_n \triangleq \frac{\sigma_n}{\sigma_1}, S \leq N$) is the number of normalized singular values above a user-defined threshold χ so that (7) holds true;

- **Step 4 - NR Excitations Optimization.** Compute the set of the *non-radiating* excitations as

$$\underline{w}^{NR} = \sum_{q=1}^{N-S} \gamma_q \underline{v}_{S+q} \quad (11)$$

where γ_q is the q -th ($q = 1, \dots, N-S$) NR expansion coefficient determined through the optimization of a user-defined cost function, $\Phi_C(\underline{w}) = \Phi_C(\underline{w}^{RA} + \underline{w}^{NR})$, that mathematically codes the additional user-defined “*non functional*” requirements on the element excitations;

- **Step 5 - CAS Problem Solution.** Determine the excitations of the array elements, \underline{w} , to be implemented in the BFN (see Appendix) by substituting (10) and (11) in (5).

4 Numerical Results

This section is devoted to illustrate the features of the proposed *NR-CAS* method and to show its performance on a set of representative *CAS* problems. Both linear (*1D*) and planar (*2D*) *PAs* as well as different “*functional*” design goals and user-defined “*non-functional*” constraints have been addressed. More specifically, the following test cases (*TCs*) have been dealt with:

- the minimization of the dynamic range ratio (*DRR*) (*TC1*);
- the presence of a “*forbidden*” region within the antenna aperture where no elementary radiating elements can be placed (*TC2*);
- the use of amplifiers with a limited number of bits, B , thus a reduced set of amplitude values for the element excitations of the *PA* (*TC3*).

The optimization of $\Phi_C(\underline{w})$ to determine the set of complex *NR* coefficients has been performed with a suitable customization of the Particle Swarm Optimizer (*PSO*) [32] by using the following calibration setup [30]: $T = N - S$ (T being the swarm dimension), $\omega = 0.4$ (ω being the inertial weight), $C_1 = C_2 = 2.0$ (C_1 and C_2 being the cognitive and the social acceleration coefficients, respectively). The initial swarm has been randomly initialized also including the null solution, namely setting $\gamma_q = 0$ ($q = 1, \dots, N - S$) in (11), and all simulations have been performed by running a non-optimized software code on a standard laptop PC at 2.4 GHz CPU with 2 GB of RAM.

In the first synthesis problem (*TC1*), the array architecture is a linear array of $N = 32$ elements located along the y -axis with a uniform inter-element spacing equal to $d = 0.3\lambda$ [i.e., $x_n = 0$, $y_n = (n - 1) \times d$ ($n = 1, \dots, N$)]. The reference power pattern, which is only function of θ due to the *1D* layout [i.e., $P^{ref}(\theta, \phi) \rightarrow P^{ref}(\theta)$], has been chosen equal to an asymmetric shaped beam, namely a cosecant-squared power pattern [Figs. 3(e)], to fulfill a mask pattern characterized by the following features: $SLL^{ref} = -20$ [dB] (SLL being the sidelobe level), $RPE = 1.0$ [dB] (RPE being the main lobe ripple), and $FNBW = 68$ [deg] ($FNBW$ being the first null beamwidth). The corresponding amplitude, $\{\alpha_n^{ref}; n = 1, \dots, N\}$, and phase, $\{\beta_n^{ref}; n = 1, \dots, N\}$, distributions of the array excitations in Figs. 3(a)-3(b) have been computed with

a linear programming (*LP*) approach [31]. According to the proposed *NR-CAS* method, the synthesis of the array excitation set, \underline{w} , starts with the definition of the *MN* excitation weights, \underline{w}^{RA} . Towards this end, the *SVD* of the linear operator \mathcal{G} has been carried out according to (9) for determining the singular values, $\{\sigma_n; n = 1, \dots, N\}$, and the corresponding sets of eigenvectors, $\mathcal{U} = \{\underline{u}_m; m = 1, \dots, M\}$ and $\mathcal{V} = \{\underline{v}_n; n = 1, \dots, N\}$. Figure 4(a) plots the normalized singular values, $\{\hat{\sigma}_n; n = 1, \dots, N\}$, that exhibit the well-known “knee” trend. The magnitude and the phase of the *MN* excitations, \underline{w}^{RA} , computed by setting different values of the *SVD* truncation threshold, χ , are reported in Figs. 4(c)-4(d), while the corresponding power patterns, $P^{RA}(\theta)|_{\chi}$, together with the reference one, $P^{ref}(\theta)$, are shown in Fig. 4(b), respectively. As expected, lower values of χ imply a better matching between $P^{RA}(\theta)$ and $P^{ref}(\theta)$. When choosing $\chi = \chi_2 = 3.5 \times 10^{-3}$ [Fig. 4(a)], the number of singular values above the threshold χ turns out to be $S = 24$ and the pattern tolerance (7) is $\xi < 10^{-4}$. The *NR* coefficients, $\{\gamma_q; q = 1, \dots, N - S\}$, have been then synthesized by means of the *PSO*-based optimization strategy through the minimization of the *DRR* thus

$$\Phi_C(\underline{w})|_{TC1} \triangleq \frac{\max_{n=1, \dots, N} \{\alpha_n\}}{\min_{n=1, \dots, N} \{\alpha_n\}}. \quad (12)$$

The magnitude and the phase of the *NR* coefficients in (11), $\{\gamma_q; q = 1, \dots, N - S\}$, of the best trial solution of the swarm at different representative iterations until the convergence ($i = I, I = 500$) are shown in Fig. 3(c) and Fig. 3(d), respectively. The corresponding element-level excitations, $\{w_n = w_n^{RA}(\chi)|_{\chi=\chi_2} + w_n^{NR}; n = 1, \dots, N\}$, and the arising power patterns are given in Figs. 3(a)-3(b) and in Fig. 3(e), respectively. For the sake of completeness, the evolution of the cost function value of the best solution of the swarm, Φ_i^{opt} ($\Phi_i^{opt} \triangleq \min_{t=1, \dots, T} \{\Phi_C([\underline{w}_t^i])\}$, $[\underline{w}_t^i]$ being the t -th trial excitation set at the i -th iteration), versus the iteration index i ($i = 0, \dots, I$) is reported in Fig. 5. As expected, the optimized *NR-CAS* solution outperforms the minimum-norm (labeled as *RA*) one in terms of the design goal ($DRR^{RA} \approx 31.55$ vs. $DRR^{NR-CAS} \approx 3.40$), while the value of the quality factor [33]

$$Q = \frac{\sum_{n=1}^N \alpha_n^2}{\int_0^\pi \int_0^{2\pi} P(\theta, \phi) \sin \theta d\theta d\phi} \quad (13)$$

slightly increases ($Q^{RA} = 0.61$ vs. $Q^{NR-CAS} = 0.75$).

In order to assess the reliability of the synthesized *NR-CAS* solution, a more realistic model for the elementary radiator, instead of an ideal one, has been considered. More specifically, the single-polarization aperture-coupled stacked square patch antenna [34] in Figs. 6(a)-6(b) and Tab. I, which resonates at $f = 3.5$ [GHz], has been chosen. In particular, the antenna consists of two stacked microstrip patch radiators printed on top of two substrates and it is fed by a microstrip line coupled through a rectangular slot. The slot is etched in a ground-plane that separates the patches and the feeding line. The dielectric material of the substrates is Rogers “RT/Duroid 3003” [35], which is characterized by a relative permittivity and a loss tangent equal to $\epsilon_r = 3.0$ and $\tan \delta = 0.0016$, respectively. The power pattern of the array layout in Fig. 6(c) has been simulated with the finite-element full-wave solver *Ansys HFSS* [36] to properly take into account mutual coupling effects. Figure 7 compares the ideal *NR-CAS* pattern and the numerically-simulated one by showing that the main deviations between the two plots only arise in the region close to end-fire (i.e., $\sin \theta = 1$), while there is a good match in the overall.

In the second test case (*TC2*), the goal is to exploit the *NR* current components to create a “forbidden” region, Ψ , within the array aperture where no array elements can be placed (Fig. 8). Towards this end, the objective cost function $\Phi_C(\underline{w})$ has been defined as follows

$$\Phi_C(\underline{w})|_{TC2} \triangleq \sum_{(x_n, y_n) \in \Psi, \forall n} \alpha_n \quad (14)$$

and the benchmark example was that of a square planar array having $N = 16 \times 16$ elements located on a regular square lattice with uniform inter-element spacing equal to $d = 0.45\lambda$ along the x and y direction. The reference power pattern is a flat-top power pattern in Fig. 9(e) with asymmetric sidelobes that fits the lower and upper masks reported in Fig. 9(a) and Fig. 9(b), respectively, featuring $RPE = 0.5$ [dB] and $FNBW = 50$ [deg] along both the x -axis and y -axis. The reference amplitude, $\{\alpha_n^{ref}; n = 1, \dots, N\}$, and phase, $\{\beta_n^{ref}; n = 1, \dots, N\}$, excitations in Fig. 9(c) and Fig. 9(d), respectively, have been again obtained through *LP*. Once performed the *SVD* of \mathcal{G} , the distribution of the normalized singular values, $\{\hat{\sigma}_n; n = 1, \dots, N\}$, is that in Fig. 10. To achieve a value of the power pattern matching error (7) $\xi < 10^{-4}$,

the threshold χ has been set to $\chi = 7.2 \times 10^{-3}$ so that the number of singular values turned out equal to $S = 236$. The synthesis of the NR coefficients, $\{\gamma_q; q = 1, \dots, N - S\}$, has been yielded by running the PSO -based optimization for $I = 2000$ iterations due to the larger number of unknowns as compared to the previous example. The behavior of the optimal value of the cost function (14), Φ_i^{opt} , during the iterative minimization is given in Fig. 11, while the magnitudes, $\{|\gamma_q|; q = 1, \dots, N - S\}$, and the phases, $\{\angle \gamma_q; q = 1, \dots, N - S\}$, of the NR coefficients of $[\underline{w}]_{opt}^i$ ($[\underline{w}]_{opt}^i$ being the best solution of the swarm at the i -th ($i = 0, \dots, I$) iteration, $[\underline{w}]_{opt}^i \triangleq \arg \left[\min_{t=1, \dots, T} \left\{ \Phi_C \left([\underline{w}]_t^i \right) \right\} \right]$) at both the iterations $i = \{0, 500, 1000\}$ and convergence ($i = I^{conv} = 1895$ since $\Phi_i^{opt}|_{i=I^{conv}} = 0$) are shown in Fig. 12(a) and Fig. 12(b), respectively.

To assess the fulfillment of the “forbidden” region constraint, let us analyze the magnitude, $\{\alpha_n; n = 1, \dots, N\}$, and the phase, $\{\beta_n; n = 1, \dots, N\}$, of the corresponding element-level excitations, $\{w_n; n = 1, \dots, N\}$, in Figs. 13(a)-13(d) and Figs. 13(e)-13(h), respectively. As expected, starting from the reference distribution [$i = 0$ - Fig. 13(a)] that violates the null-excitations condition in the whole area Ψ , the solution improves during the iterations [Figs. 13(b)-13(c)] until the convergence [Fig. 13(d)] when $\Phi_C \left([\underline{w}]_{opt}^{I^{conv}} \right) = 0$. On the other hand, the excitations profile in Fig. 13(d) and Fig. 13(h) radiates a power pattern whose cuts along the principal planes, $\phi = 0$ [deg] and $\phi = 90$ [deg], are reported in Fig. 12(c) and Fig. 12(d), respectively, to confirm the mask-matching of the NR -CAS solution.

Analogously to the test case $TC1$, the reliability of the synthesis process has been checked also here by considering the same radiator [Figs. 6(a)-6(b)] to simulate with *Ansys HFSS* [36] the non-ideal planar array in Fig. 14. The comparison between the ideal and the full-wave NR -CAS patterns along $\phi = 0$ [deg] [Fig. 15(a)] and $\phi = 90$ [deg] [Fig. 15(b)] highlights that also in this case, the main deviations from the ideal behavior occur far from broadside and within the sidelobe region.

The last test case ($TC3$) is concerned with the use of the proposed NR -based method to simplify the BFN . Accordingly, digital amplifiers with $B = 2$ bits have been considered so that only four (i.e., $2^B|_{B=2} = 4$) possible amplitude values were available: $\underline{\alpha}^{trg} = \{0.25, 0.50, 0.75, 1.00\}$. As for the array, the layout of the previous example ($TC2$) has been kept, but setting different

lower and upper masks for the reference power [Figs. 16(a)-16(b)] with $RPE = 1.0$ [dB] and $FNBW = 45$ [deg] in both Cartesian planar axes. Therefore, the LP -computed excitations are those in Figs. 16(c)-16(d), while the corresponding reference flat-top power pattern is shown in Fig. 16(e). Since the array geometry is the same of $TC2$, the entries of \mathcal{G} (8) do not change as well as the normalized singular values, $\{\sigma_n; n = 1, \dots, N\}$ (Fig. 10) and the eigenvectors, $\mathcal{U} = \{\underline{u}_m; m = 1, \dots, M\}$ and $\mathcal{V} = \{\underline{v}_n; n = 1, \dots, N\}$. Moreover, the same values of χ and S (i.e., $\chi = 7.2 \times 10^{-3}$ and $S = 236$) have been used, as well. The minimization of the cost function to enforce quantized amplitude excitations

$$\Phi_C(\underline{w})|_{TC3} = \sum_{n=1}^N \min_{i=1, \dots, 2^B} |\alpha_n - \alpha_i^{trg}| \quad (15)$$

stops after $i = I^{conv} = 1651$ iterations (Fig. 17). Figure 18 shows the evolution of both the NR coefficients [Figs. 18(a)-18(b)] of $[\underline{w}]_{opt}^i$ and the radiated patterns [Figs. 18(c)-18(d)] during the iterative optimization, while the corresponding element-level excitations, $\{w_n; n = 1, \dots, N\}$, are reported in Fig. 19 in terms of magnitude (16), $\{\alpha_n; n = 1, \dots, N\}$ [Figs. 19(a)-19(d)], and phase (17), $\{\beta_n; n = 1, \dots, N\}$ [Figs. 19(e)-19(h)], coefficients. By observing the magnitude terms on the left column of Fig. 19, one can notice that thanks to the NR contribution, $\{w_n^{NR}; n = 1, \dots, N\}$, the convergence ($i = I^{conv} = 1651$) amplitudes [Fig. 19(d)] are quantized to the target values [i.e., $\alpha_n \in \{0.25, 0.50, 0.75, 1.00\}$ ($n = 1, \dots, N$)]. Of course, this does not impact on the pattern radiated by the array as confirmed by the pictures of the principal cuts of the power pattern in Figs. 18(c)-18(d). Lastly, the good agreement with the prediction given by the full-wave simulator (Fig. 20) further assesses the reliability of the NR -CAS synthesis.

5 Conclusions and Final Remarks

An innovative method, namely the NR -CAS approach, for the constrained synthesis of PA antennas has been proposed. It is aimed at synthesizing the complex (amplitude and phase) excitations of the array elements to fulfill “*non-functional*” constraints, while fitting desired power pattern masks. More specifically, the array weights are expressed as the linear combination of a radiating minimum-norm term, to enforce the “*functional*” far-field behavior, and a NR

component that generates a null *EM* field outside the array aperture, but allows one to properly address other requirements on the array structure. The synthesis of the *NR* term is yielded by determining its expansion coefficients with respect to a set of basis functions derived from the *SVD* of the radiation operator. Towards this end, an optimization problem is formulated by defining a suitable cost function, which mathematically quantifies the degree of fulfillment of the “*non-functional*” constraints, to be minimized according to a *PSO*-based iterative process. From the numerical assessment, the following main outcomes can be drawn:

- the *NR-CAS* method is a versatile technique able to properly handle the constrained synthesis of the *PA* excitations such as the optimization of the *DRR*, the inclusion of a “*forbidden*” region within the array aperture, and the use of digital amplifiers with only few amplitude levels;
- the *NR-CAS* method is computationally very efficient since the synthesis is concerned with a number of *DoFs* [i.e., the $(N - S)$ *NR* expansion coefficients] much smaller than those of a standard design, which is equal to the number of antenna array elements, the *DoFs* being the whole set of N array excitations.

Future research activities, beyond the scope of this work, will be aimed at extending the proposed *NR-CAS* method to other array geometries and/or architectures (e.g., unconventional arrays [3]) as well as different types of “*non-functional*” constraints or requirements.

Appendix

The complex excitation, w_n ($w_n = \alpha_n e^{j\beta_n}$), of the n -th ($n = 1, \dots, N$) radiating element of the *PA*, is obtained from the corresponding n -th ($n = 1, \dots, N$) *radiating*, w_n^{RA} ($w_n^{RA} = \alpha_n^{RA} e^{j\beta_n^{RA}}$), and *non-radiating*, w_n^{NR} ($w_n^{NR} = \alpha_n^{NR} e^{j\beta_n^{NR}}$), components. More specifically, the n -th ($n = 1, \dots, N$) amplitude coefficient α_n is given by

$$\alpha_n = \sqrt{(\alpha_n^{RA})^2 + 2\alpha_n^{NR}\alpha_n^{RA} [\cos(\beta_n^{RA} - \beta_n^{NR})] + (\alpha_n^{NR})^2}, \quad (16)$$

while the n -th ($n = 1, \dots, N$) phase term β_n is yielded as follows

$$\beta_n = \arctan \left(\frac{\alpha_n^{RA} \sin \beta_n^{RA} + \alpha_n^{NR} \sin \beta_n^{NR}}{\alpha_n^{RA} \cos (\beta_n^{RA}) + \alpha_n^{NR} \cos (\beta_n^{NR})} \right). \quad (17)$$

Acknowledgements

This work benefited from the networking activities carried out within the Project DICAM-EXC (Grant L232/2016) funded by the Italian Ministry of Education, Universities and Research (MUR) within the 'Departments of Excellence 2023-2027' Program (CUP: E63C22003880001). Moreover, it benefited from the networking activities carried out within the Project SEME@TN - Smart ElectroMagnetic Environment in TrentiNo funded by the Autonomous Province of Trento (CUP: C63C22000720003), the Project AURORA - Smart Materials for Ubiquitous Energy Harvesting, Storage, and Delivery in Next Generation Sustainable Environments funded by the Italian Ministry for Universities and Research within the PRIN-PNRR 2022 Program (CUP: E53D23014760001), the Project National Centre for HPC, Big Data and Quantum Computing (CN HPC) funded by the European Union - NextGenerationEU within the PNRR Program (CUP: E63C22000970007), the Project Telecommunications of the Future [PE00000001 - program RESTART, Project 6GWINET (CUP: D43C22003080001), Project MOSS (CUP: J33C22002880001), Project IN (CUP: J33C22002880001), Project EMS-MMDV (CUP: J33C22002880001), Project TRIBOLETTO (CUP: B53C22003970001), and Project SMART (CUP: E63C22002040007)], funded by European Union under the Italian National Recovery and Resilience Plan (NRRP) of NextGenerationEU, and the support of the Natural Science Basic Research Program of Shaanxi Province (Grants No. 2022-JC-33, No. 2023-GHZD-35, and No. 2024JC-ZDXM-25). Views and opinions expressed are however those of the author(s) only and do not necessarily reflect those of the European Union or the European Research Council. Neither the European Union nor the granting authority can be held responsible for them. A. Massa wishes to thank E. Vico for her never-ending inspiration, support, guidance, and help.

References

- [1] R. L. Haupt and Y. Rahmat-Samii, "Antenna array developments: A perspective on the past, present and future," *IEEE Antennas Propag. Mag.*, vol. 57, no. 1, pp. 86-96, Feb. 2015.
- [2] J. S. Herd and M. D. Conway, "The evolution to modern phased array architectures," *IEEE Proc.*, vol. 104, no. 3, pp. 519-529, Mar. 2016.
- [3] P. Rocca, G. Oliveri, R. J. Mailloux, and A. Massa, "Unconventional phased array architectures and design methodologies - A review," *IEEE Proc.*, vol. 104, no. 3, pp. 544-560, Mar. 2016.
- [4] R. S. Elliott, *Antenna Theory Design*. Hoboken, NJ, USA: Wiley, 2003.
- [5] R. L. Haupt, *Antenna Arrays - A Computation Approach*. Hoboken, NJ, USA: Wiley, 2010.
- [6] R. J. Mailloux, *Phased Array Antenna Handbook*. Norwood, MA, USA: Artech House, 2018.
- [7] N. Anselmi, L. Tosi, P. Rocca, G. Toso, and A. Massa, "A self-replicating single-shape tiling technique for the design of highly modular planar phased arrays - The case of L-shaped rep-tiles," *IEEE Trans. Antennas Propag.*, vol. 71, no. 4, pp. 3335-3348, Apr. 2023.
- [8] J.-Y. Chen, Z.-H. Xu, W. Dong, and S.-P. Xiao, "Optimization of module partition based on the weighted clustering method for a wideband irregular subarrayed array," *IEEE Trans. Antennas Propag.*, vol. 71, no. 7, pp. 5817-5827, Jul. 2023.
- [9] Y. Lee, "Clustered and thinned antenna array for adaptive interference suppression via k-medoids of desired-signal steering vector," *IEEE Trans. Antennas Propag.*, vol. 72, no. 3, pp. 2867-2872, Mar. 2024.
- [10] L. Poli, G. Oliveri, N. Anselmi, A. Benoni, L. Tosi, and A. Massa, "Unconventional array design in the autocorrelation domain - Isophoric 1D thinning," *IEEE Trans. Antennas Propag.*, 2025 (DOI: 10.1109/TAP.2025.3595902).

- [11] P. Rocca, F. Yang, L. Poli, and S. Yang, "Time-modulated array antennas - Theory, techniques, and applications," *J. Electromagn. Waves Appl.*, vol. 33, no. 12, pp. 1503-1531, 2019.
- [12] Z. Zhu, Y. Chen, Y. Feng, and S. Yang, "Fast pattern synthesis for large-scale time-modulated planar arrays with a novel two-stage iterative convex optimization method," *IEEE Trans. Antennas Propag.*, vol. 72, no. 5, pp. 4636-4641, May 2024.
- [13] M. Bertero and P. Boccacci, *Introduction to Inverse Problems in Imaging*. Bristol, U.K.: IOP Press, 1998.
- [14] J. A. Kong, *Electromagnetic Wave Theory*. Cambridge, MA, USA: EMW Publishing, 2008.
- [15] W. C. Chew, Y. M. Wang, G. Otto, D. Lesselier, and J. C. Bolomey, "On the inverse source method of solving inverse scattering problems," *Inv. Prob.*, vol. 10, pp. 547-553, 1994.
- [16] S. Caorsi and G. L. Gragnani, "Inverse scattering method for dielectric objects based on the reconstruction of nonmeasurable equivalent current density," *Radio Sci.*, vol. 34, no. 1, pp. 1-8, Jan. 1999.
- [17] B. Fuchs, L. L. Coq, and M. D. Migliore, "Fast antenna array diagnosis from a small number of far-field measurements," *IEEE Trans. Antennas Propag.*, vol. 64, no. 6, pp. 2227-2235, Jun. 2016.
- [18] M. Salucci, A. Gelmini, G. Oliveri, and A. Massa, "Planar arrays diagnosis by means of an advanced Bayesian compressive processing," *IEEE Trans. Antennas Propag.*, vol. 66, no. 11, pp. 5892-5906, Nov. 2018.
- [19] A. J. Devaney and E. Wolf, "Radiating and nonradiating classical current distributions and the fields they generate," *Phys. Rev. D Part. Fields*, vol. 8, no. 4, pp. 1044-1047, Aug. 1973.
- [20] N. Bleistein and J. K. Cohen, "Nonuniqueness in the inverse source problem in acoustics and electromagnetics," *J. Math. Phys.*, vol. 18, no. 2, pp. 194-201, Feb. 1977.

- [21] E. A. Marengo and R. W. Ziolkowski, "Nonradiating and minimum energy sources and their fields: generalized source inversion theory and applications," *IEEE Trans. Antennas Propag.*, vol. 48, no. 10, pp. 1553-1562, Oct. 2000.
- [22] O. M. Bucci and G. Franceschetti, "On the degrees of freedom of scattered fields," *IEEE Trans. Antennas Propag.*, vol. 37, no. 7, pp. 918-926, Jul. 1989.
- [23] M. Salucci, A. Gelmini, G. Oliveri, N. Anselmi, and A. Massa, "Synthesis of shaped beam reflectarrays with constrained geometry by exploiting non-radiating surface currents," *IEEE Trans. Antennas Propag.*, vol. 66, no. 11, pp. 5805-5817, Nov. 2018.
- [24] M. Salucci, G. Oliveri, and A. Massa, "An innovative inverse source approach for the feasibility-driven design of reflectarrays," *IEEE Trans. Antennas Propag.*, vol. 70, no. 7, pp. 5468-5480, Jul. 2022.
- [25] G. Oliveri, F. Zardi, and A. Massa, "On the improvement of the performance of inexpensive electromagnetic skins by means of an inverse source design approach," *IEEE Trans. Antennas Propag.*, vol. 73, no. 5, pp. 3284-3295, May 2025.
- [26] A. Massa, A. Benoni, P. Da Ru, S. K. Goudos, B. Li, G. Oliveri, A. Polo, P. Rocca, and M. Salucci, "Designing smart electromagnetic environments for next-generation wireless communications," *Telecom*, vol. 2, no. 2, pp. 213-221, 2021.
- [27] F. Yang, D. Erricolo, and A. Massa, "Guest Editorial - Smart Electromagnetic Environment," *IEEE Trans. Antennas Propag.*, vol. 70, no. 10, pp. 8687-8690, Oct. 2022.
- [28] T. M. Habashy, M. L. Oristaglio, and A. T. de Hoop, "Simultaneous nonlinear reconstruction of two-dimensional permittivity and conductivity," *Radio Sci.*, vol. 29, no. 4, pp. 1101-1118, Jul. 1994.
- [29] P. Rocca, M. Donelli, G. L. Gragnani, and A. Massa, "Iterative multi-resolution retrieval of non-measurable equivalent currents for the imaging of dielectric objects," *Inv. Prob.*, vol. 25, pp. 1-15, 2009.

- [30] P. Rocca, M. Benedetti, M. Donelli, D. Franceschini, and A. Massa, "Evolutionary optimization as applied to inverse scattering problems," *Inv. Prob.*, vol. 24, pp. 1-41, 2009.
- [31] T. Isernia, O. M. Bucci, and N. Fiorentino, "Shaped beam antenna synthesis problems: Feasibility criteria and new strategies," *J. Electromagn. Waves Appl.*, vol. 12, no. 1, pp. 103-138, Jan. 1998.
- [32] J. Robinson and Y. Rahmat-Samii, "Particle swarm optimization in electromagnetics," *IEEE Trans. Antennas Propag.*, vol. 52, no. 2, pp. 397-407, Feb. 2004.
- [33] R. C. Hansen, *Electrically Small, Superdirective, and Superconducting Antennas*. Hoboken, NJ, USA: Wiley, 2006.
- [34] S. D. Targonski, R. B. Waterhouse, and D. M. Pozar, "Design of wideband aperture-stacked path microstrip antennas," *IEEE Trans. Antennas Propag.*, vol. 46, no. 9, pp. 1246-1251, Sep. 1998.
- [35] Rogers Co., RO3000 Series Circuit Materials: RO3003 TM, RO3006 TM, RO3010 TM, and RO3035TM - High Frequency Laminates, USA, 2022. Accessed: 10-01-2024. [Online]. Available: <https://www.rogerscorp.com/advanced-electronics-solutions/ro3000-series-laminates/ro3003-laminates>.
- [36] ANSYS Electromagnetics Suite-HFSS, ANSYS, Canonsburg, PA, USA, 2021.

FIGURE CAPTIONS

- **Figure 1.** Sketch of a 2D array geometry.
- **Figure 2.** Flowchart of the NR-CAS method.
- **Figure 3.** *TC1 DRR Optimization* (1D Array, $N = 32$, $d = 0.3\lambda$, Coscant-squared Pattern, $SLL^{ref} = -20$ [dB], $RPE = 1.0$ [dB], $FNBW = 68$ [deg]) - Plot of (a)(c) the magnitude and (b)(d) the phase of (a)(b) the excitations of the array, $\{w_n; n = 1, \dots, N\}$, and (c)(d) the NR expansion coefficients, $\{\gamma_q; q = 1, \dots, N-S\}$, and (e) the corresponding power patterns, $P(\theta)$, at different representative iterations (i being the iteration index) of the PSO-based optimization process.
- **Figure 4.** *TC1 DRR Optimization* (1D Array, $N = 32$, $d = 0.3\lambda$, Coscant-squared Pattern, $SLL^{ref} = -20$ [dB], $RPE = 1.0$ [dB], $FNBW = 68$ [deg]) - Plot of (a) the normalized singular values of \mathcal{G} , $\{\hat{\sigma}_n; n = 1, \dots, N\}$, (c) the magnitude and (d) the phase of the minimum-norm element excitations, $\{w_n^{RA}; n = 1, \dots, N\}$, and (b) the corresponding power patterns, $P(\theta)$, in correspondence with different values of the SVD truncation threshold, χ .
- **Figure 5.** *TC1 DRR Optimization* (1D Array, $N = 32$, $d = 0.3\lambda$, Coscant-squared Pattern, $SLL^{ref} = -20$ [dB], $RPE = 1.0$ [dB], $FNBW = 68$ [deg]) - Plot of the evolution the cost function value of the best solution of the swarm, Φ_i^{opt} ($\Phi_i^{opt} \triangleq \min_{t=1, \dots, T} \left\{ \Phi_C \left([\underline{w}]_t^i \right) \right\}$, $[\underline{w}]_t^i$ being the t -th trial excitation set at the i -th iteration), versus the iteration index i ($i = 0, \dots, I; I = 500$).
- **Figure 6.** *TC1 DRR Optimization* (1D Array, $N = 32$, $d = 0.3\lambda$, Coscant-squared Pattern, $SLL^{ref} = -20$ [dB], $RPE = 1.0$ [dB], $FNBW = 68$ [deg]) - Sketch of (a) the exploded view and (b) the top view of the aperture-coupled stacked square patch antenna together with (c) the HFSS model of the array layout.
- **Figure 7.** *TC1 DRR Optimization* (1D Array, $N = 32$, $d = 0.3\lambda$, Coscant-squared Pattern, $SLL^{ref} = -20$ [dB], $RPE = 1.0$ [dB], $FNBW = 68$ [deg]) - Comparison between the ideal NR-CAS pattern and the HFSS numerically-simulated one.

- **Figure 8.** *TC2 Forbidden Region* (2D Array, $N = 16 \times 16$, $d = 0.45\lambda$, Flat-top Pattern, Asymmetric Sidelobes, $RPE = 0.5$ [dB], $FNBW = 50$ [deg]) - Sketch of the array layout with a “forbidden” region, Ψ .
- **Figure 9.** *TC2 Forbidden Region* (2D Array, $N = 16 \times 16$, $d = 0.45\lambda$, Flat-top Pattern, Asymmetric Sidelobes, $RPE = 0.5$ [dB], $FNBW = 50$ [deg]) - Plot of (a) the lower, $LM(\theta, \phi)$, and (b) the upper, $UM(\theta, \phi)$, power pattern masks, (c) the magnitude and (d) the phase of the array reference excitations, $\{w_n^{ref}; n = 1, \dots, N\}$, along with (e) the corresponding power pattern, $P^{ref}(\theta, \phi)$.
- **Figure 10.** *TC2 Forbidden Region* (2D Array, $N = 16 \times 16$, $d = 0.45\lambda$, Flat-top Pattern, Asymmetric Sidelobes, $RPE = 0.5$ [dB], $FNBW = 50$ [deg]) - Plot of the normalized singular values of \mathcal{G} , $\{\hat{\sigma}_n; n = 1, \dots, N\}$.
- **Figure 11.** *TC2 Forbidden Region* (2D Array, $N = 16 \times 16$, $d = 0.45\lambda$, Flat-top Pattern, Asymmetric Sidelobes, $RPE = 0.5$ [dB], $FNBW = 50$ [deg]) - Plot of the evolution the cost function value of the best solution of the swarm, Φ_i^{opt} ($\Phi_i^{opt} \triangleq \min_{t=1, \dots, T} \left\{ \Phi_C \left([\underline{w}]_t^i \right) \right\}$, $[\underline{w}]_t^i$ being the t -th trial excitation set at the i -th iteration), versus the iteration index i ($i = 0, \dots, I$; $I = 2000$; $I^{conv} = 1895$).
- **Figure 12.** *TC2 Forbidden Region* (2D Array, $N = 16 \times 16$, $d = 0.45\lambda$, Flat-top Pattern, Asymmetric Sidelobes, $RPE = 0.5$ [dB], $FNBW = 50$ [deg]) - Plot of (a) the magnitude and (b) the phase of the NR expansion coefficients, $\{\gamma_q; q = 1, \dots, N - S\}$, and (c) the corresponding cuts of the power pattern, $P(\theta, \phi)$, in the (c) $\phi = 0$ [deg] and (d) $\phi = 90$ [deg] planes at different representative iterations (i being the iteration index) of the PSO -based optimization process.
- **Figure 13.** *TC2 Forbidden Region* (2D Array, $N = 16 \times 16$, $d = 0.45\lambda$, Flat-top Pattern, Asymmetric Sidelobes, $RPE = 0.5$ [dB], $FNBW = 50$ [deg]) - Plot of (a)-(d) the magnitude and (e)-(h) the phase of the element excitations, $\{w_n; n = 1, \dots, N\}$, at the i -th iteration of the PSO -based optimization process: (a)(e) $i = 0$, (b)(f) $i = 500$, (c)(g) $i = 1000$, and (d)(h) $i = I^{conv}$ ($I^{conv} = 1895$).

- **Figure 14.** *TC2 Forbidden Region (2D Array, $N = 16 \times 16$, $d = 0.45\lambda$, Flat-top Pattern, Asymmetric Sidelobes, $RPE = 0.5$ [dB], $FNBW = 50$ [deg])* - Sketch of the *HFSS* model of the array layout.
- **Figure 15.** *TC2 Forbidden Region (2D Array, $N = 16 \times 16$, $d = 0.45\lambda$, Flat-top Pattern, Asymmetric Sidelobes, $RPE = 0.5$ [dB], $FNBW = 50$ [deg])* - Comparison between the ideal *NR-CAS* pattern and the *HFSS* numerically-simulated one along the planes: (a) $\phi = 0$ [deg] and (b) $\phi = 90$ [deg].
- **Figure 16.** *TC3 Quantized Amplitudes (2D Array, $N = 16 \times 16$, $d = 0.45\lambda$, Flat-top Pattern, $SLL^{ref} = -20$ [dB], $RPE = 1.0$ [dB], $FNBW = 45$ [deg])* - Plot of (a) the lower, $LM(\theta, \phi)$, and (b) the upper, $UM(\theta, \phi)$, power pattern masks, (c) the magnitude and (d) the phase of the array reference excitations, $\{w_n^{ref}; n = 1, \dots, N\}$, along with (e) the corresponding power pattern, $P^{ref}(\theta, \phi)$.
- **Figure 17.** *TC3 Quantized Amplitudes (2D Array, $N = 16 \times 16$, $d = 0.45\lambda$, Flat-top Pattern, $SLL^{ref} = -20$ [dB], $RPE = 1.0$ [dB], $FNBW = 45$ [deg])* - Plot of the evolution the cost function value of the best solution of the swarm, Φ_i^{opt} ($\Phi_i^{opt} \triangleq \min_{t=1, \dots, T} \left\{ \Phi_C \left([\underline{w}]_t^i \right) \right\}$, $[\underline{w}]_t^i$ being the t -th trial excitation set at the i -th iteration), versus the iteration index i ($i = 0, \dots, I$; $I = 2000$; $I^{conv} = 1651$).
- **Figure 18.** *TC3 Quantized Amplitudes (2D Array, $N = 16 \times 16$, $d = 0.45\lambda$, Flat-top Pattern, $SLL^{ref} = -20$ [dB], $RPE = 1.0$ [dB], $FNBW = 45$ [deg])* - Plot of (a) the magnitude and (b) the phase of the *NR* expansion coefficients, $\{\gamma_q; q = 1, \dots, N - S\}$, and (c) the corresponding cuts of the power pattern, $P(\theta, \phi)$, in the (c) $\phi = 0$ [deg] and (d) $\phi = 90$ [deg] planes at different representative iterations (i being the iteration index) of the *PSO*-based optimization process.
- **Figure 19.** *TC3 Quantized Amplitudes (2D Array, $N = 16 \times 16$, $d = 0.45\lambda$, Flat-top Pattern, $SLL^{ref} = -20$ [dB], $RPE = 1.0$ [dB], $FNBW = 45$ [deg])* - Plot of (a)-(d) the magnitude and (e)-(h) the phase of the element excitations, $\{w_n; n = 1, \dots, N\}$, at the i -th iteration of the *PSO*-based optimization process: (a)(e) $i = 0$, (b)(f) $i = 100$, (c)(g) $i = 500$, and (d)(h) $i = I^{conv}$ ($I^{conv} = 1651$).

- **Figure 20.** *TC3 Quantized Amplitudes* (2D Array, $N = 16 \times 16$, $d = 0.45\lambda$, Flat-top Pattern, $SLL^{ref} = -20$ [dB], $RPE = 1.0$ [dB], $FNBW = 45$ [deg]) - Comparison between the ideal *NR-CAS* pattern and the *HFSS* numerically-simulated one along the planes: (a) $\phi = 0$ [deg] and (b) $\phi = 90$ [deg].

TABLE CAPTIONS

- **Table I.** Aperture-coupled stacked square patch antenna descriptors.

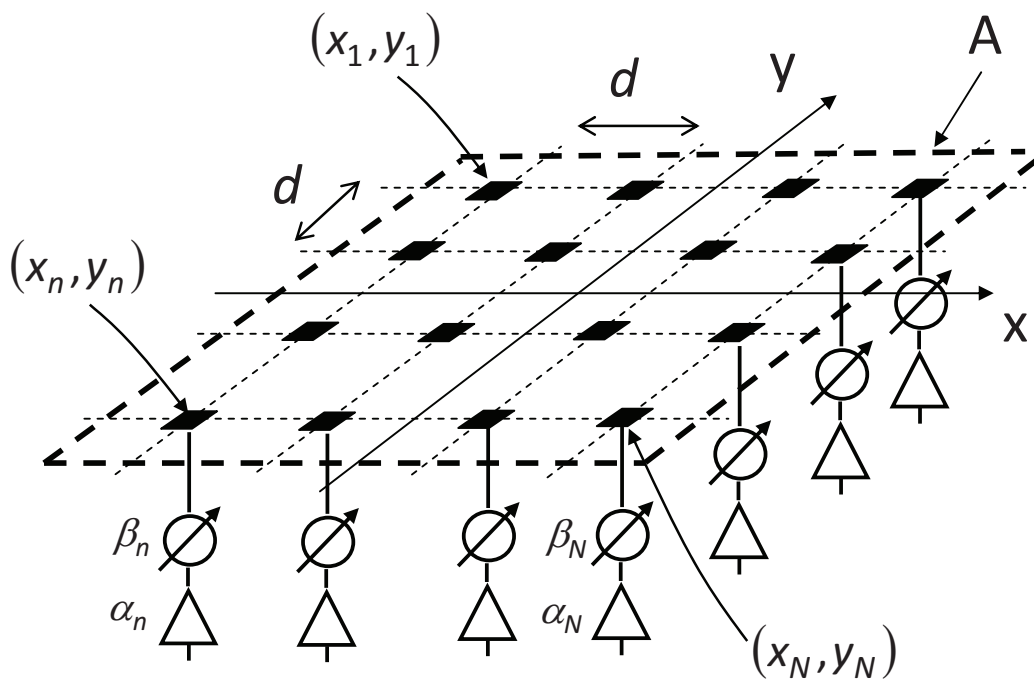


Fig. 1 - Poli *et al.*, “Inverse Source Method for Constrained Phased Array Synthesis ...”

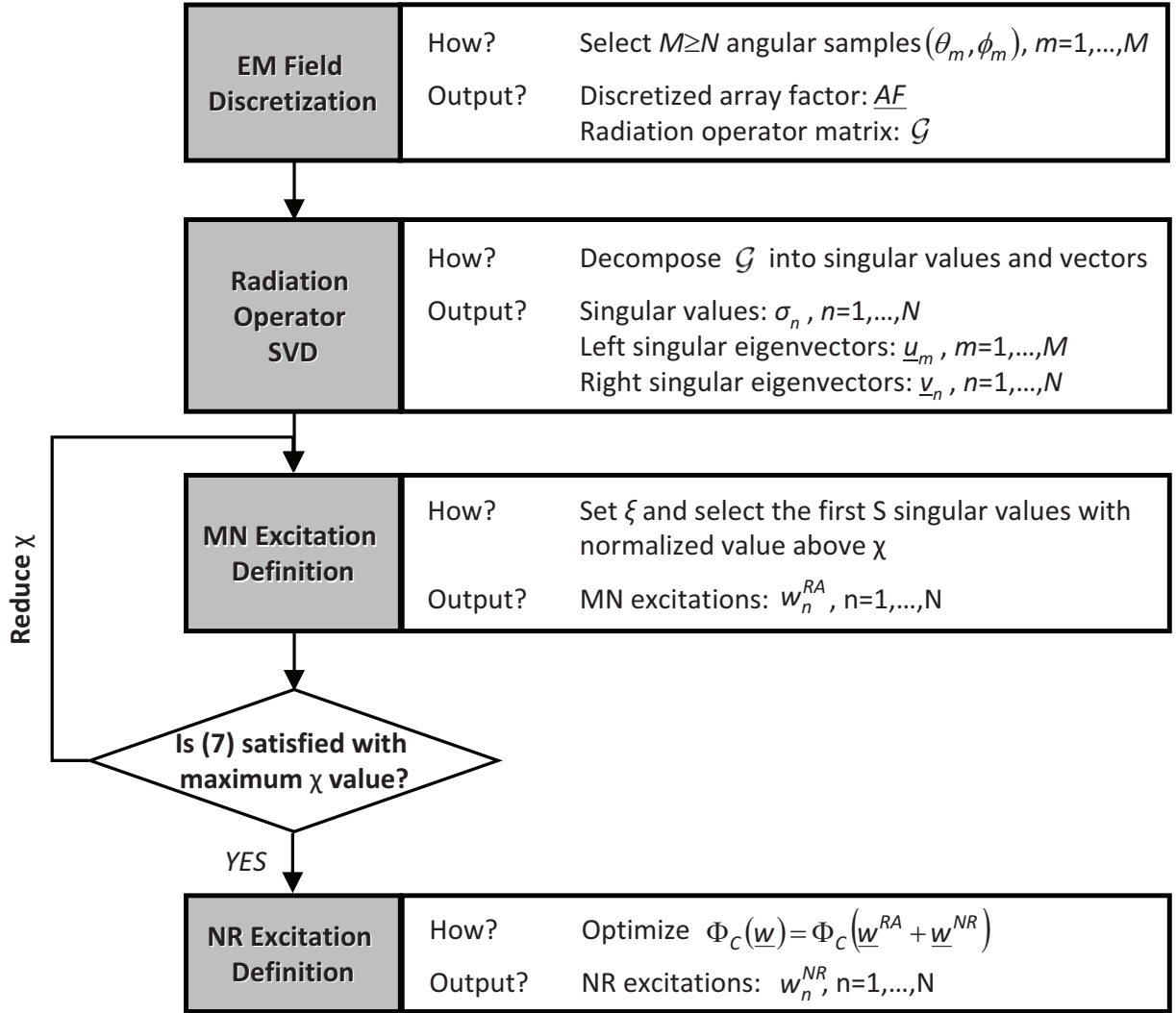


Fig. 2 - Poli *et al.*, “Inverse Source Method for Constrained Phased Array Synthesis ...”

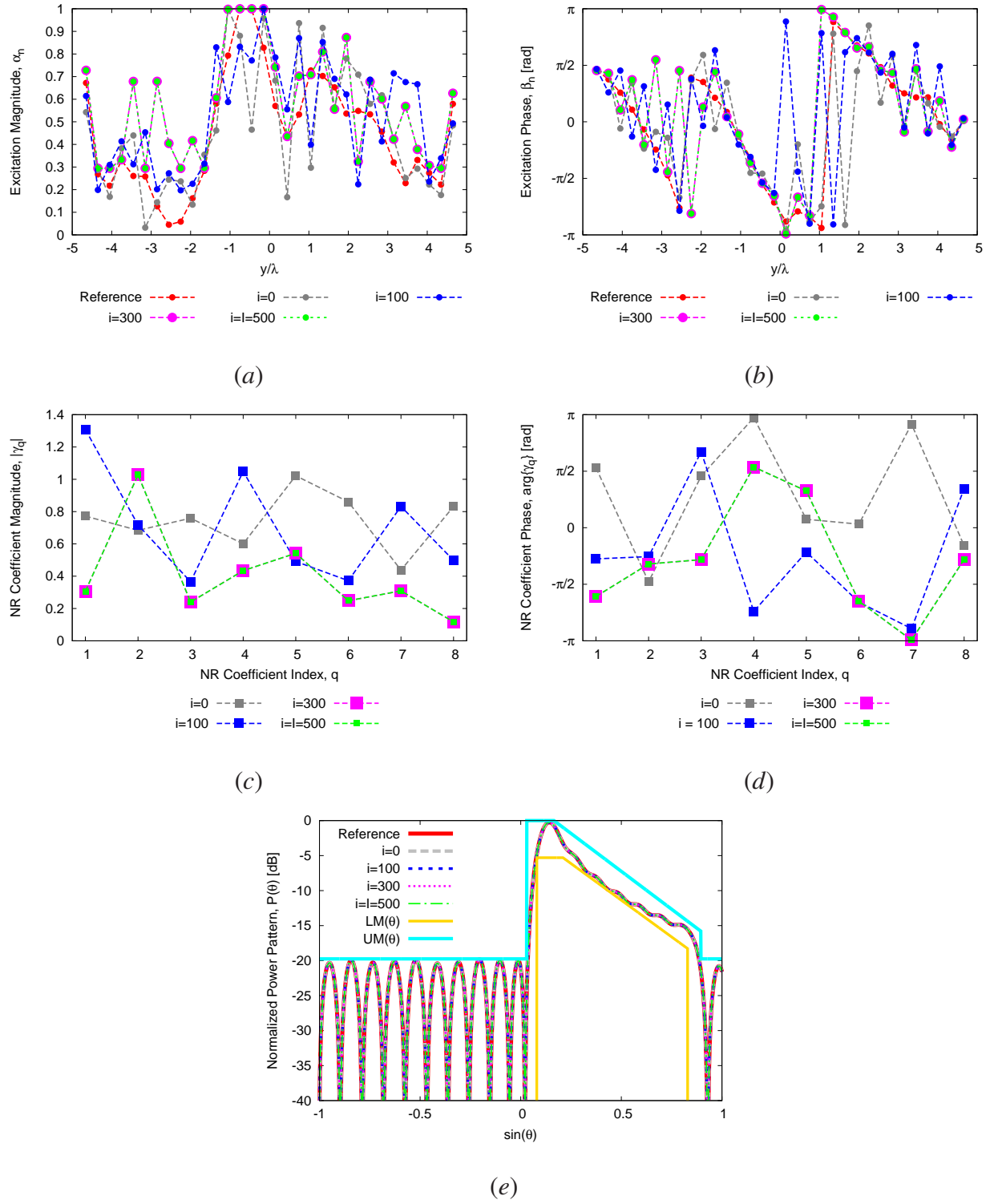
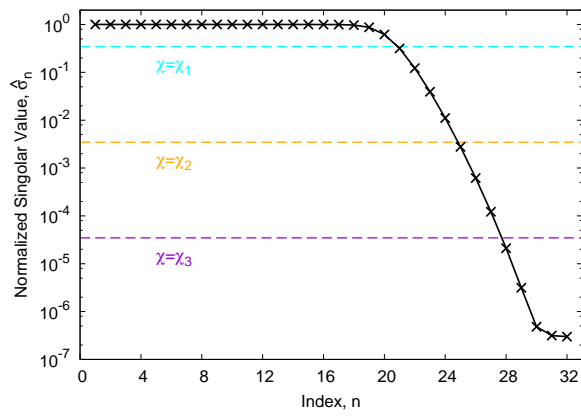
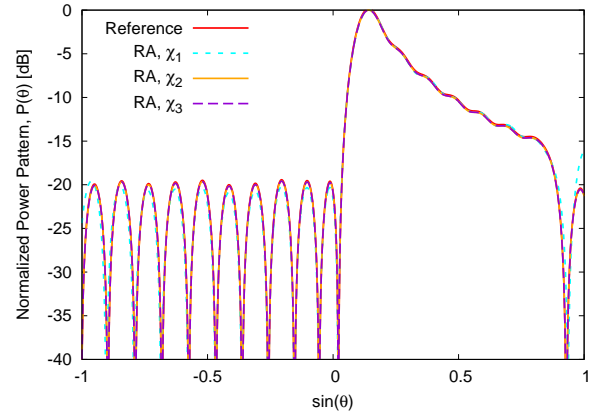


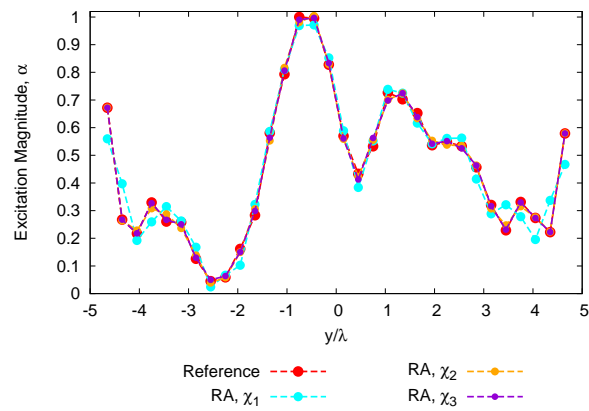
Fig. 3 - Poli *et al.*, “Inverse Source Method for Constrained Phased Array Synthesis ...”



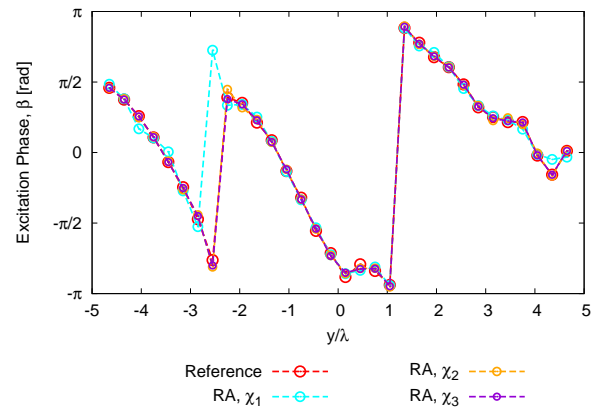
(a)



(b)



(c)



(d)

Fig. 4 - Poli *et al.*, “Inverse Source Method for Constrained Phased Array Synthesis ...”

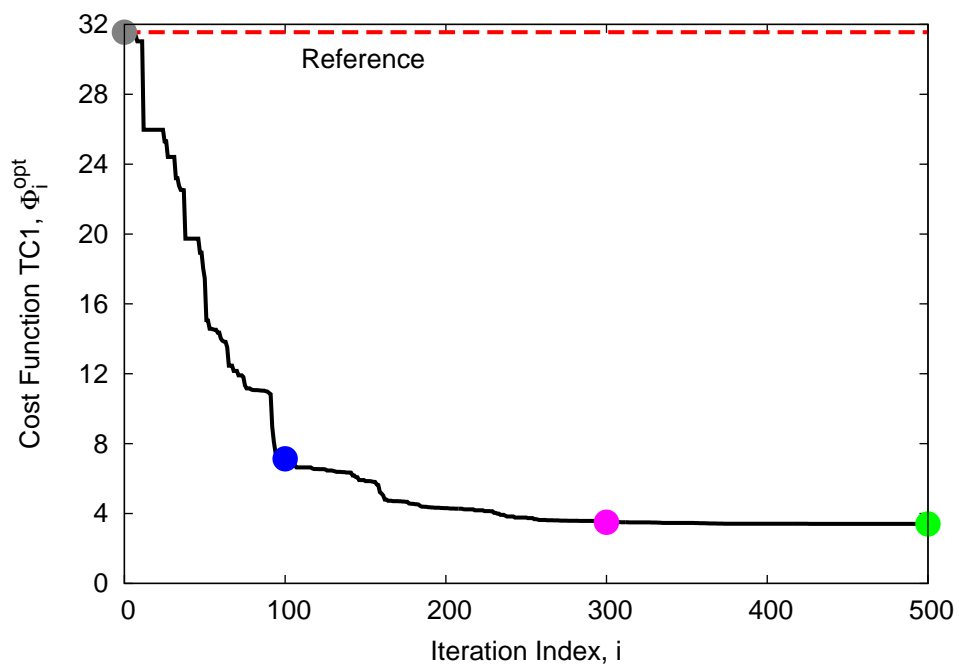


Fig. 5 - Poli *et al.*, “Inverse Source Method for Constrained Phased Array Synthesis ...”

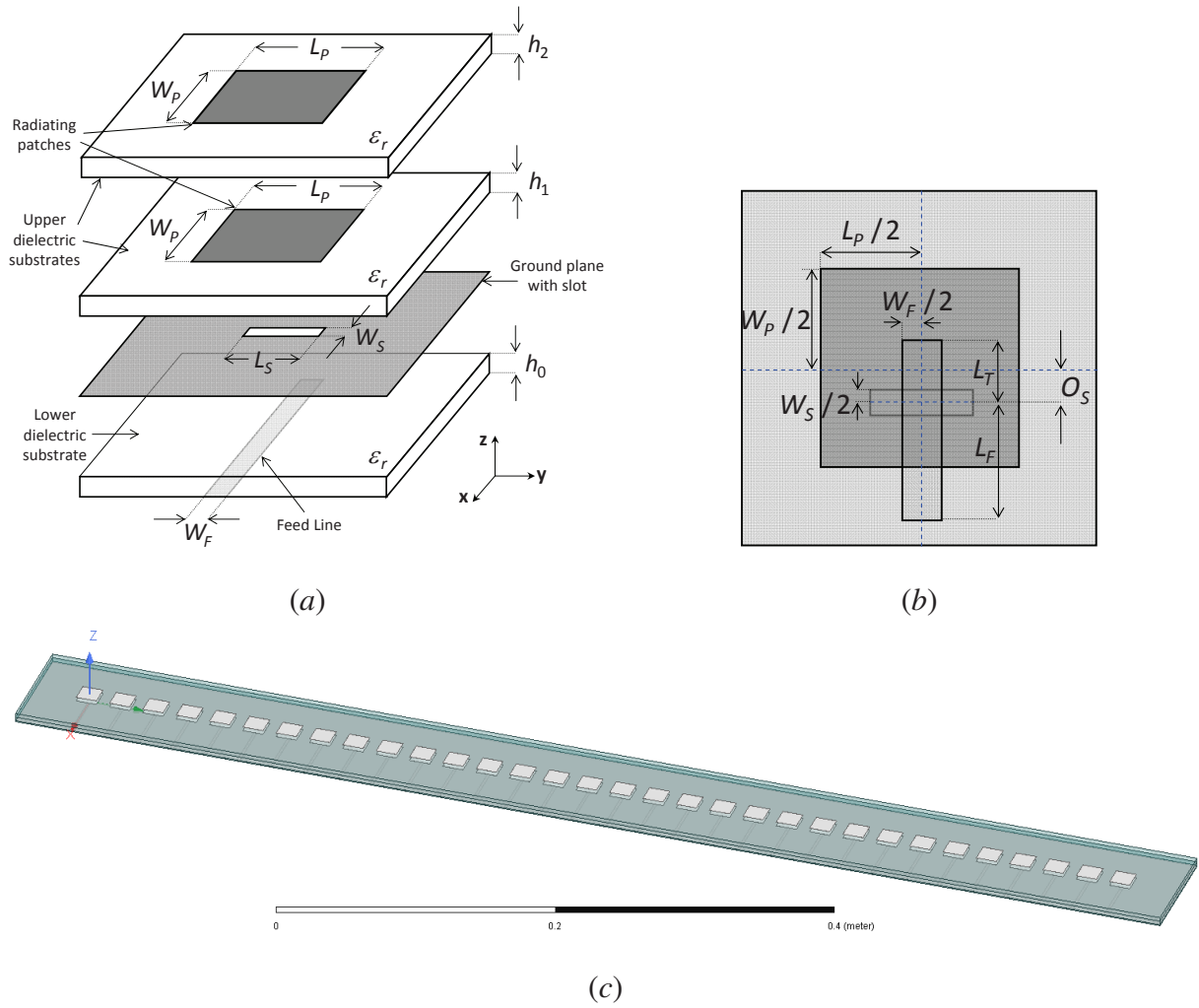


Fig. 6 - Poli *et al.*, “Inverse Source Method for Constrained Phased Array Synthesis ...”

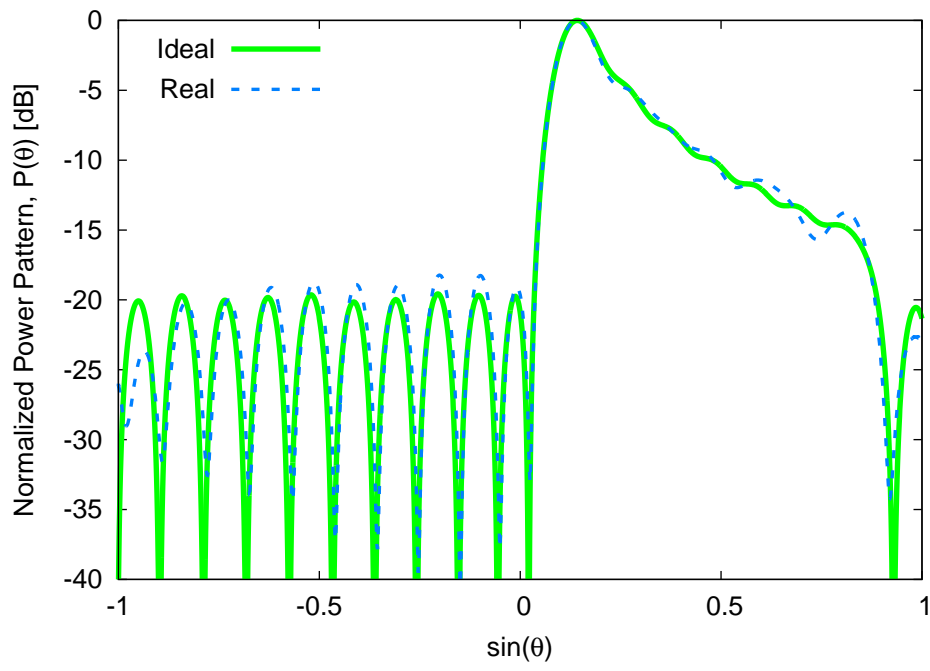


Fig. 7 - Poli *et al.*, “Inverse Source Method for Constrained Phased Array Synthesis ...”

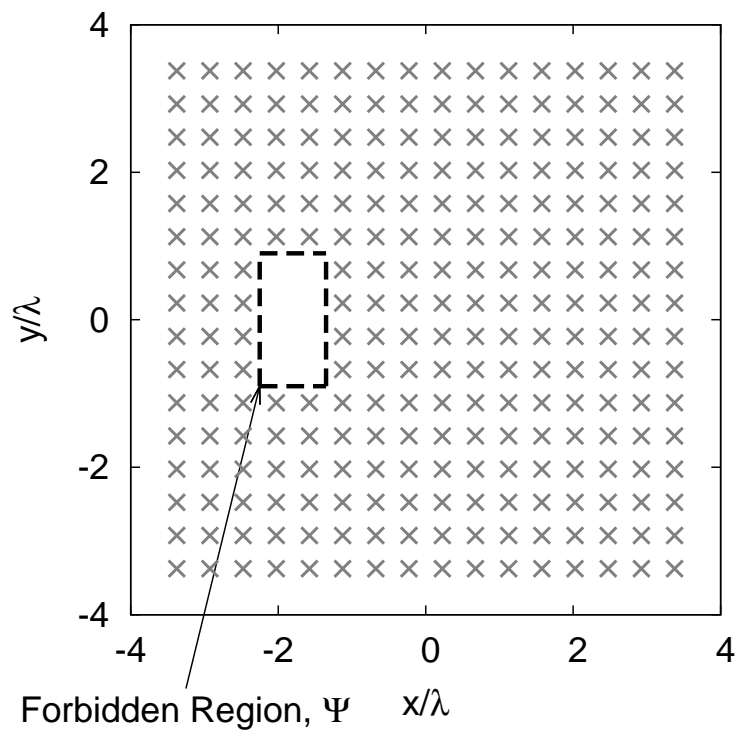


Fig. 8 - Poli *et al.*, “Inverse Source Method for Constrained Phased Array Synthesis ...”

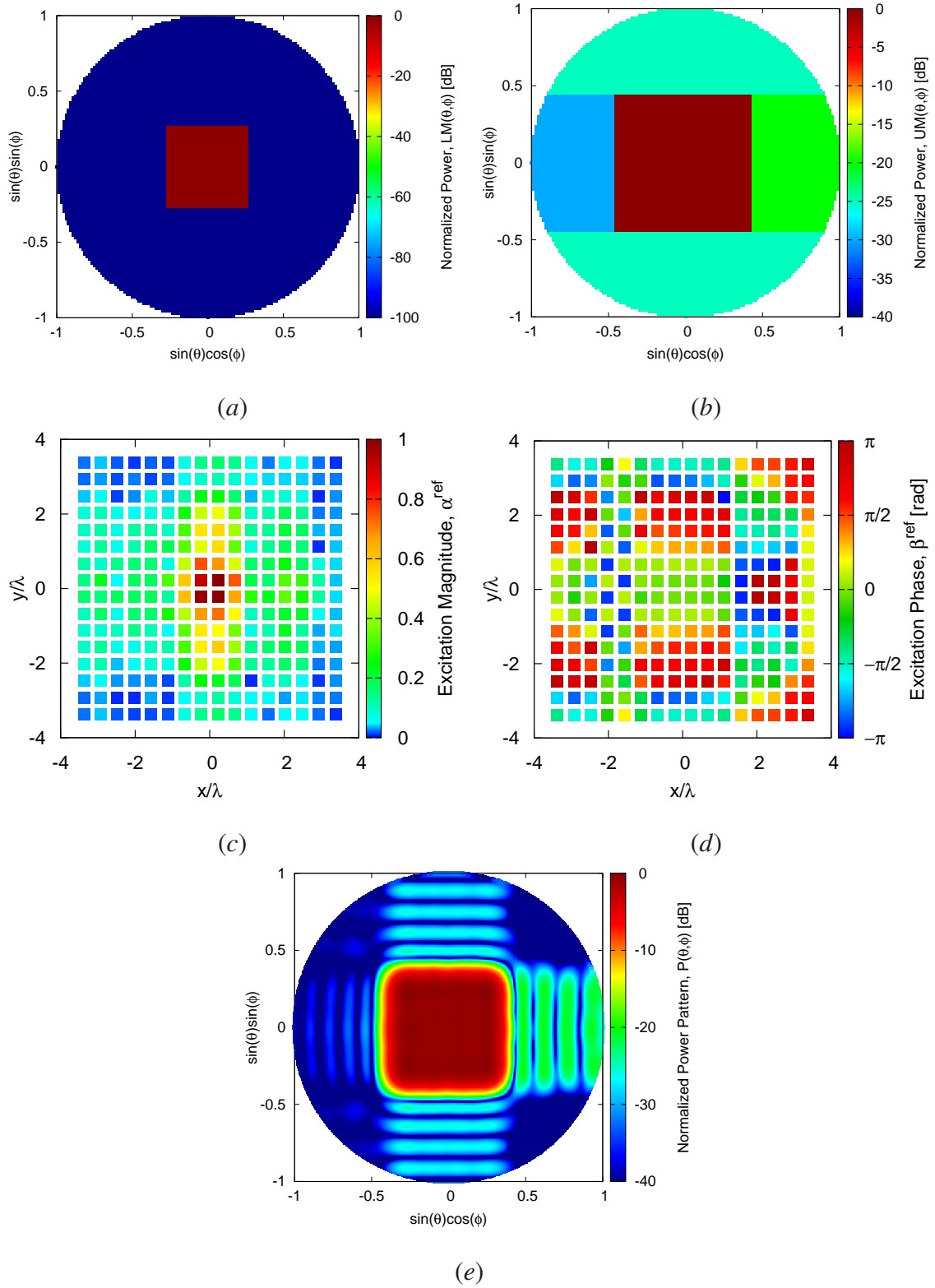


Fig. 9 - Poli *et al.*, “Inverse Source Method for Constrained Phased Array Synthesis ...”

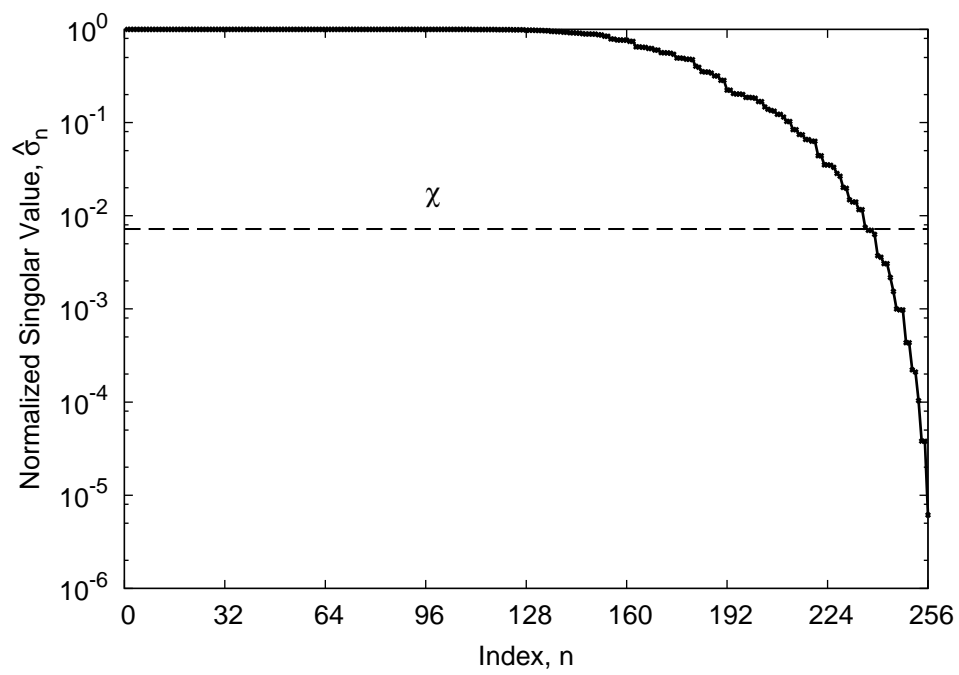


Fig. 10 - Poli *et al.*, “Inverse Source Method for Constrained Phased Array Synthesis ...”

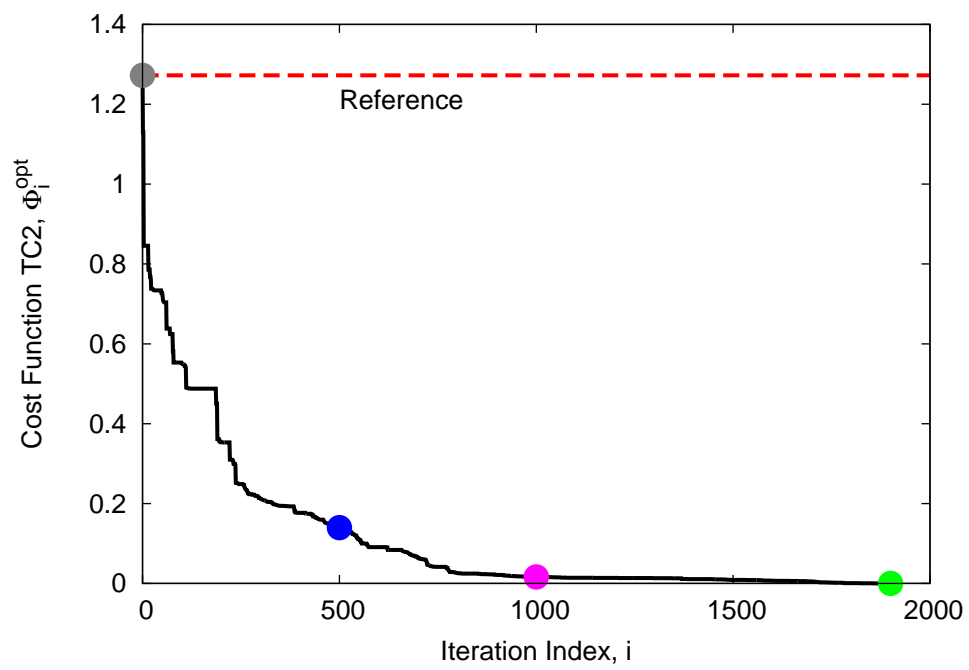
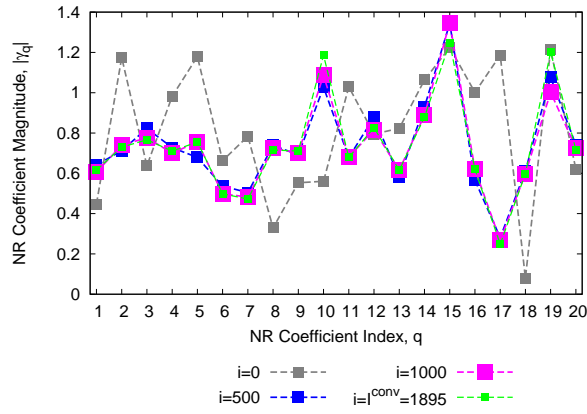
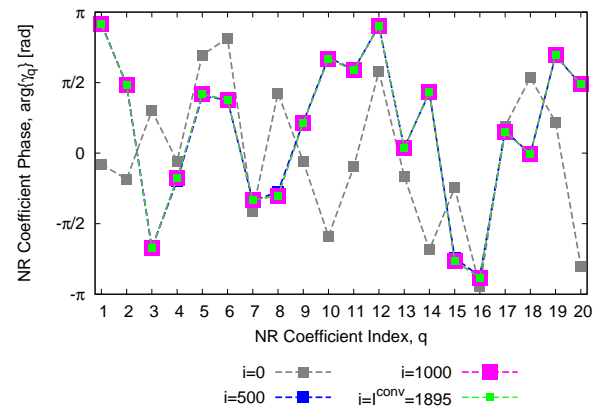


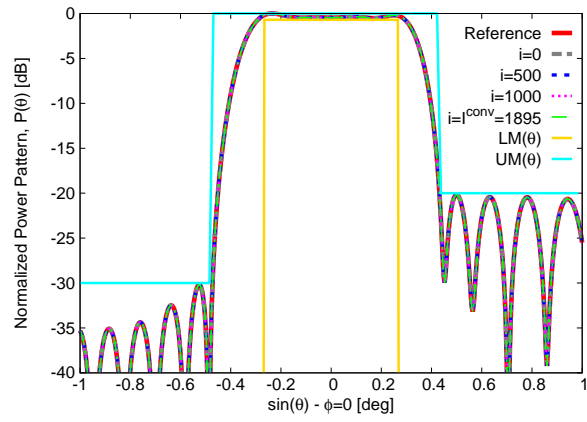
Fig. 11 - Poli *et al.*, “Inverse Source Method for Constrained Phased Array Synthesis ...”



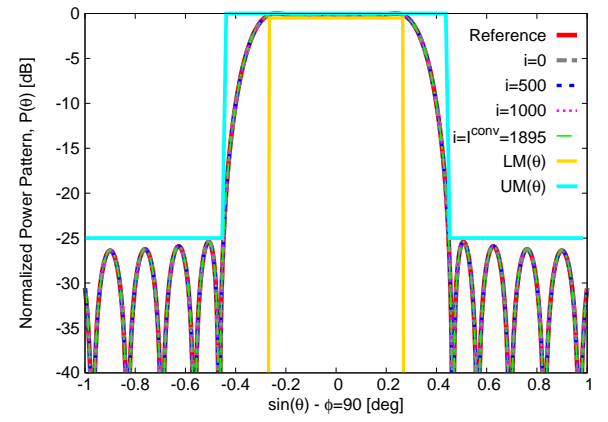
(a)



(b)



(c)



(d)

Fig. 12 - Poli *et al.*, “Inverse Source Method for Constrained Phased Array Synthesis ...”

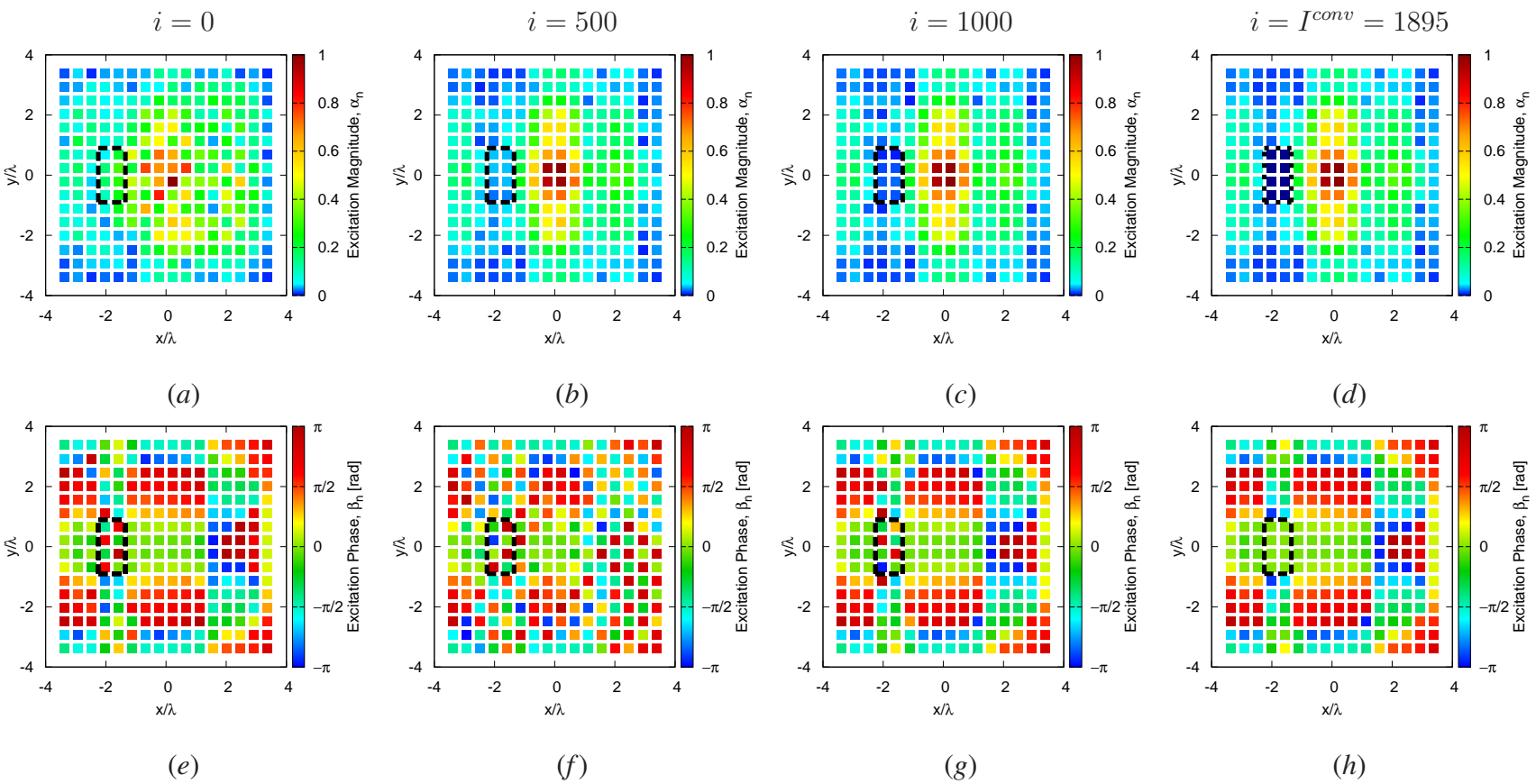


Fig. 13 - Poli *et al.*, “Inverse Source Method for Constrained Phased Array Synthesis ...”

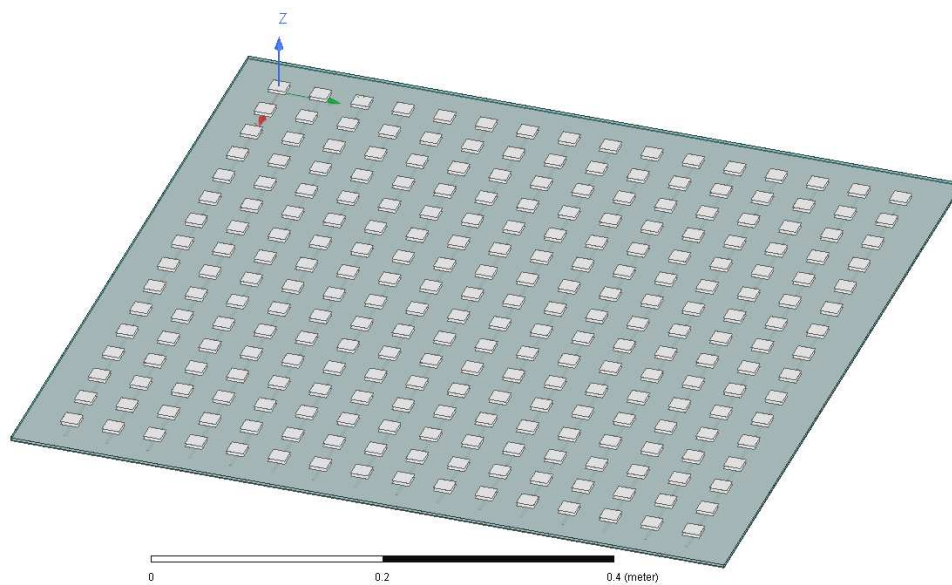
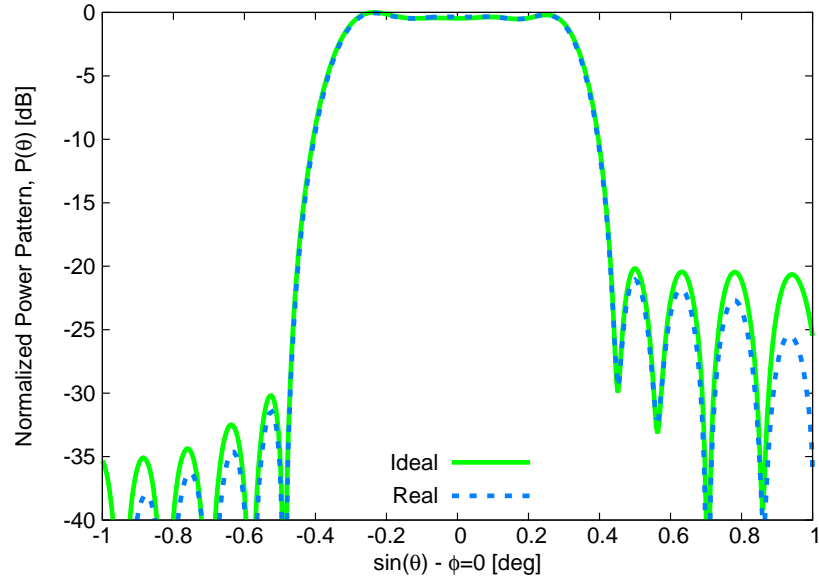
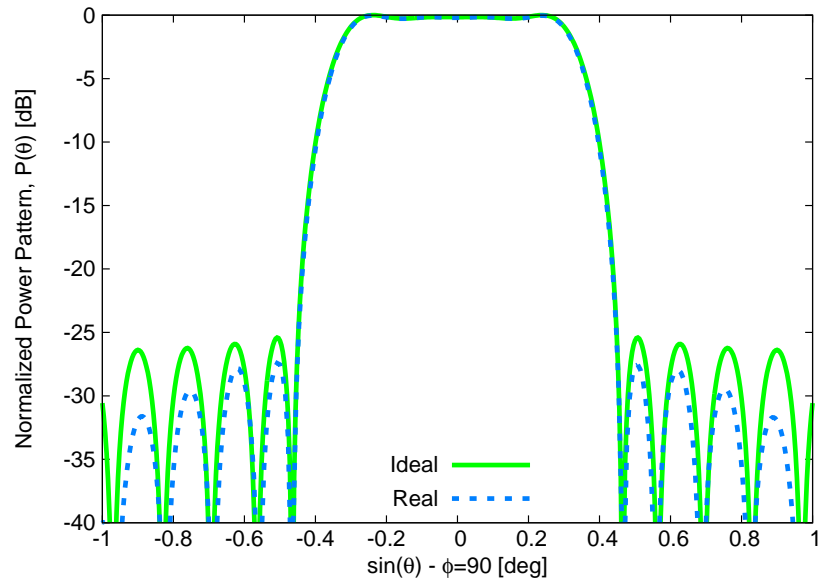


Fig. 14 - Poli *et al.*, “Inverse Source Method for Constrained Phased Array Synthesis ...”



(a)



(b)

Fig. 15 - Poli *et al.*, “Inverse Source Method for Constrained Phased Array Synthesis ...”

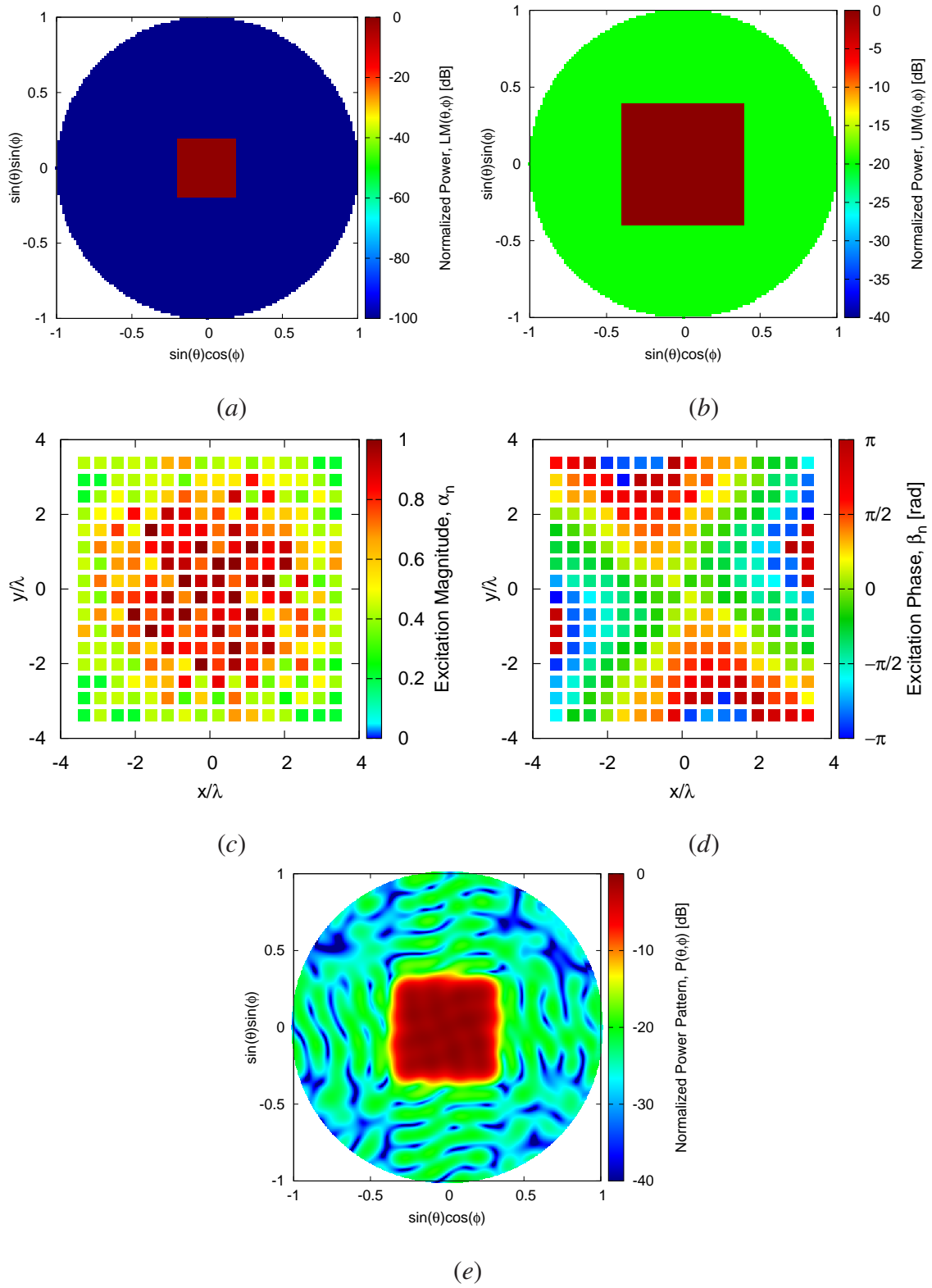


Fig. 16 - Poli *et al.*, “Inverse Source Method for Constrained Phased Array Synthesis ...”

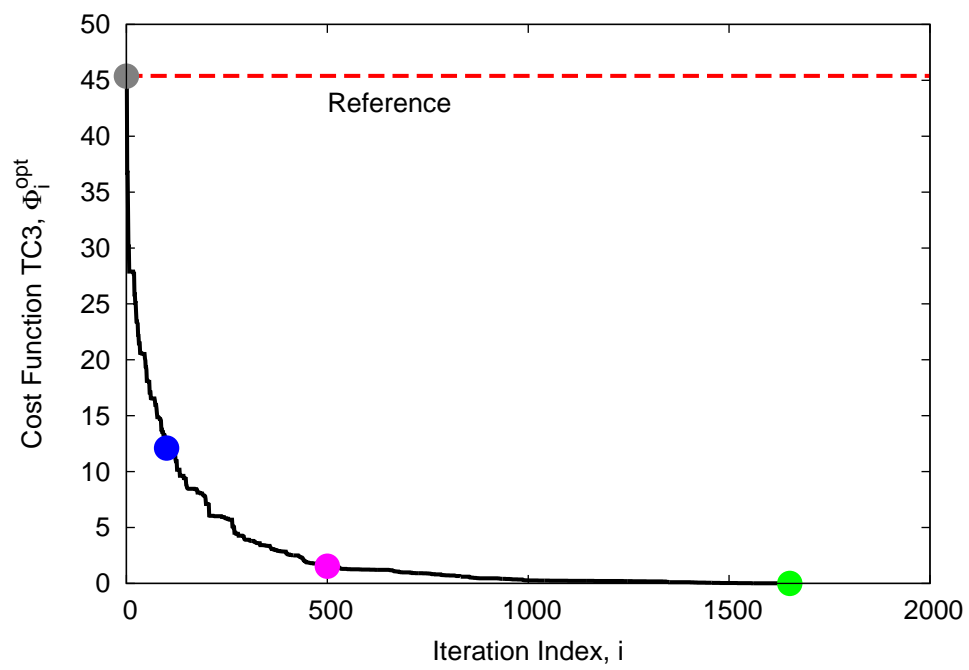


Fig. 17 - Poli *et al.*, “Inverse Source Method for Constrained Phased Array Synthesis ...”

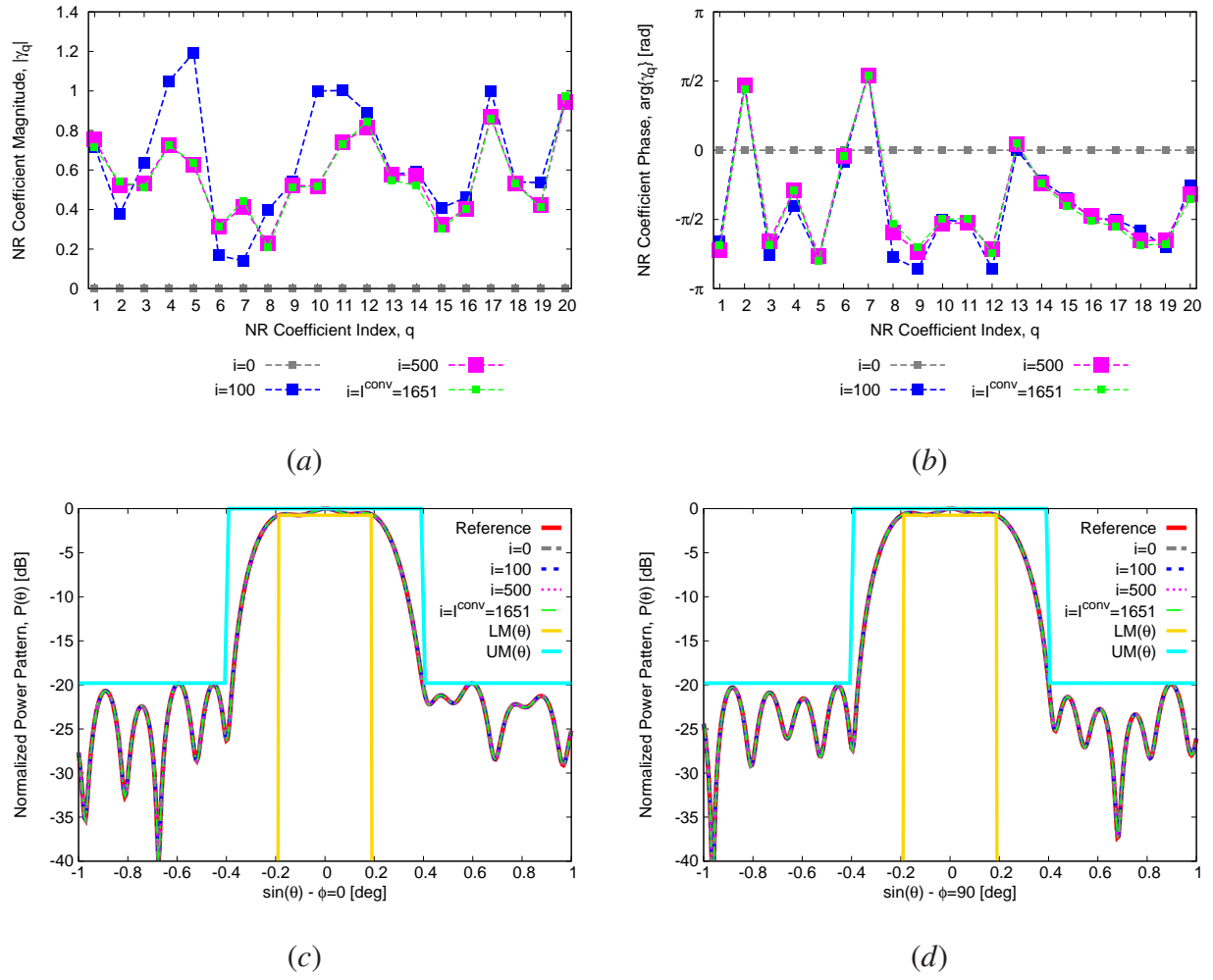


Fig. 18 - Poli *et al.*, “Inverse Source Method for Constrained Phased Array Synthesis ...”

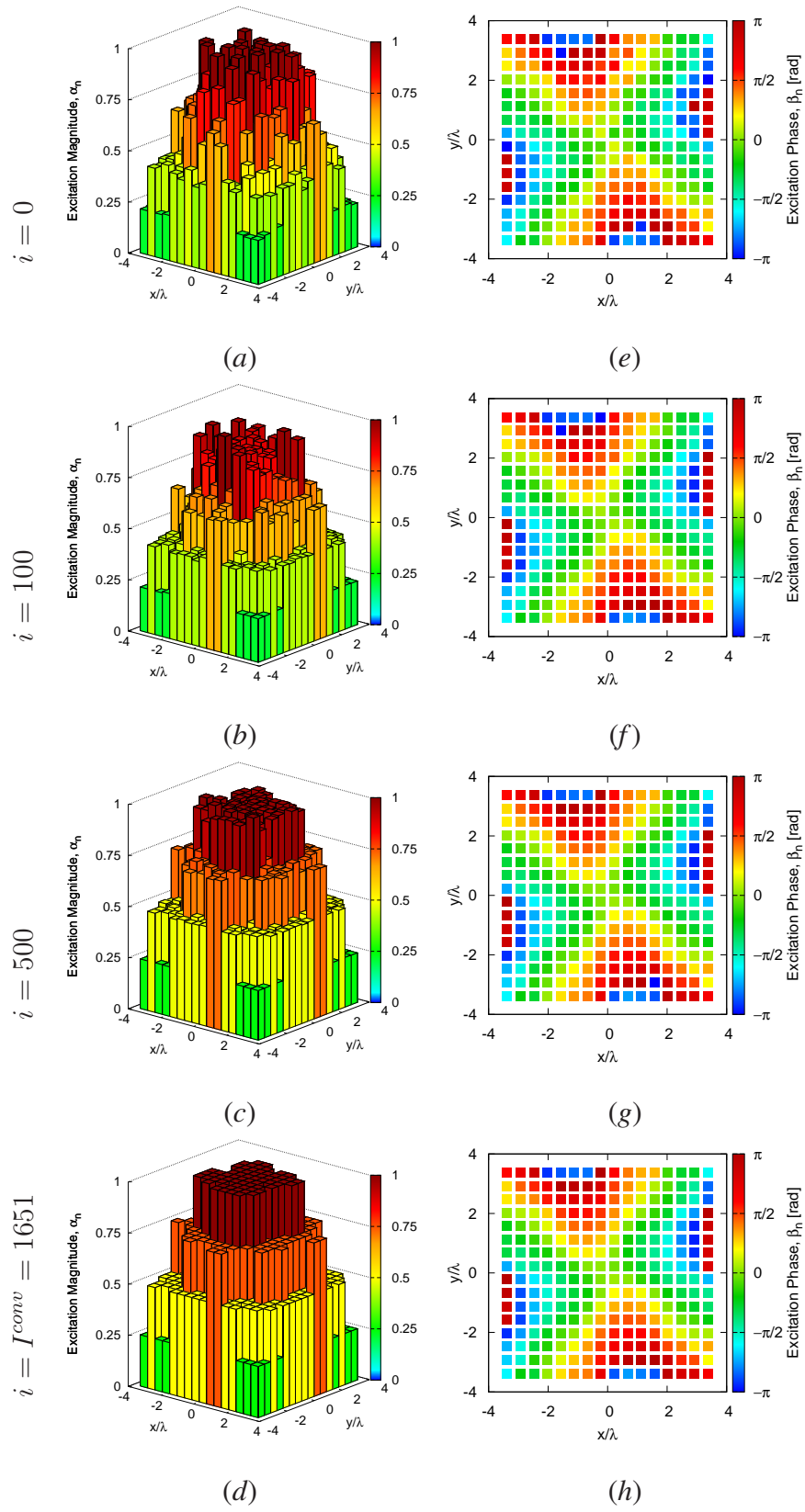
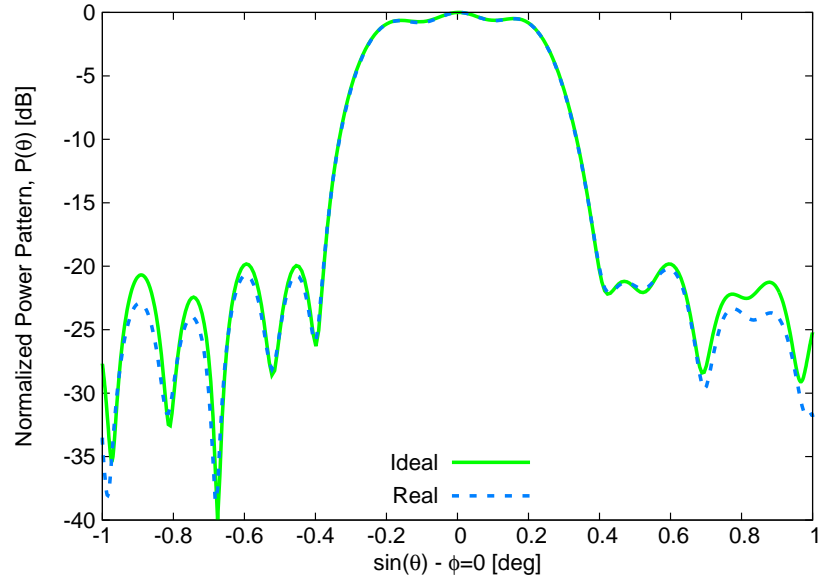
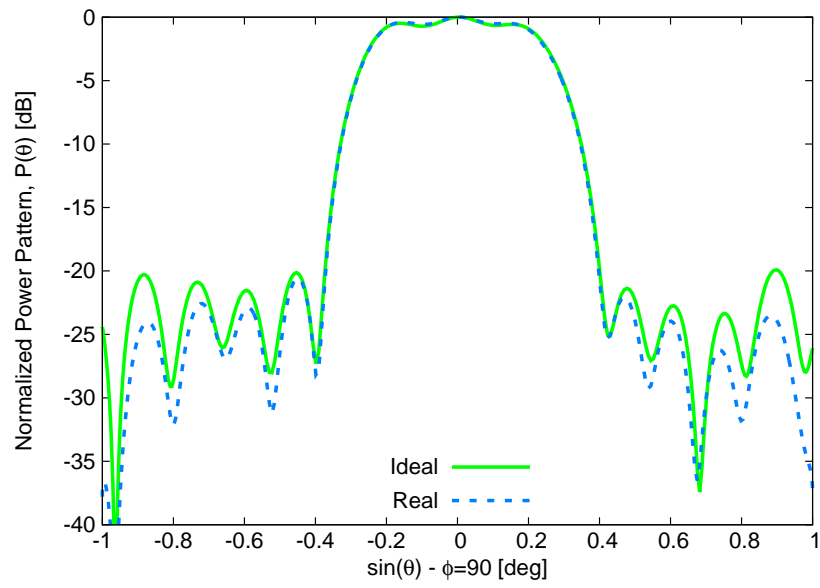


Fig. 19 - Poli *et al.*, “Inverse Source Method for Constrained Phased Array Synthesis ...”



(a)



(b)

Fig. 20 - Poli *et al.*, “Inverse Source Method for Constrained Phased Array Synthesis ...”

<i>Parameter</i>	<i>Value</i>
h_0	7.60×10^{-4} [m]
h_1	4.56×10^{-3} [m]
h_2	4.56×10^{-3} [m]
$h_p = h_G$	3.50×10^{-5} [m]
$LP = WP$	2.04×10^{-2} [m]
WF	4.08×10^{-3} [m]
L_F	4.66×10^{-3} [m]
L_T	3.51×10^{-3} [m]
O_S	1.60×10^{-3} [m]
WS	5.94×10^{-3} [m]
LS	2.04×10^{-2} [m]
ε_r	3.0
$\tan \delta$	1.6×10^{-3}

Tab. I - Poli *et al.*, “Inverse Source Method for Constrained Phased Array Synthesis ...”